universität wien

MASTERARBEIT / MASTER'S THESIS

Titel der Masterarbeit / Title of the Master's Thesis

„Simulation of kinetically limited self-assembly of colloidal particles with mobile surface DNA linkers “

verfasst von / submitted by

Leah Rank, BSc

angestrebter akademischer Grad / in partial fulfilment of the requirements for the degree of

Master of Science (MSc)

Wien, 2023 / Vienna, 2023

Studienkennzahl lt. Studienblatt / degree programme code as it appears on the student record sheet:	UA 066 876
Studienrichtung lt. Studienblatt / degree programme as it appears on the student record sheet:	Masterstudium Physics UG2002
Betreut von / Supervisor:	Dr. Pedro A. Sánchez

Contents

1 Introduction

Studying the self-organization of matter forming complex systems has always been of great interest in the scientific world. The topic unites physicists, chemists, and biologists. It is the reason why living organisms were able to form and eventually evolve into thinking humans. [1, 2] The phenomenon can be observed on many different length scales: From molecules to cells, bacteria, and even swarms of insects, fish, or birds [3]. Self-assembling systems are able to form some kind of global order due to enthalpic and entropic factors competing locally which can be observed and ideally quantified by an order parameter. They became the focus when trying to understand the mechanisms behind certain (biological) processes. In recent years, artificial self-assembling systems have been created to replicate and therefore study the self-organization occurring in nature but also to develop functional materials without human interaction [4] on different length scales with numerous different shapes of particles and bonding mechanisms [5] [6]. The main idea when designing these so-called supramolecular systems is to limit the bonding valence, *i.e.*, to only enable certain connective mechanisms between particles that come with well-defined directional and/or selective interactions which eventually result in specific predictable overall system properties that can be exploited for various purposes [7]. Depending on the desired global characteristics, *i.e.*, the configurations after self-assembly, the local interactions amongst the particles as well as their shape can be tuned. Self-assembling particles can even be used for drug delivery in cancer research [8]. When forming surfaces these systems can serve as filters or sensors [9, 10].

Colloidal suspensions have drawn scientists' attention since in many aspects, they scale up compared to atomistic systems. But because of their size, they are much easier to observe and their phase behavior can be tuned more precisely [7, 11, 12, 13]. Equipping colloidal particles with bonding mechanisms enables them to form targeted connections amongst each other which could lead to clustered formations that may, for instance, function as biosensors [14]. In literature, many approaches are discussed when creating these binding colloids, for example by adding hydrophobic or charged patches [7, 6]. Here, the focus lies on a recent [15] and very promising way to form self-assembling particles: DNA-coated colloids (DNACCs) where DNA strands, so-called linkers, attached to the colloids are able to form hybridization bonds with other compatible strands and thereby establish connections with other colloids [7, 11, 16, 17, 18, 19, 20, 21, 22]. These systems naturally appear to be interesting because they are extremely versatile and DNA is a convenient tool when aiming for target-oriented or selective bonding. Since DNA hybridization bonds, illustrated in figure 2, are sensitive to temperature they make DNACCs hold an additional tuning aspect. Above a certain threshold temperature T_h, the base pairs detach, allowing the formation of the clustered configurations to be reversible. The temperature reversibility makes it possible to tune the system's rheology quite easily by heating or cooling the solvent. [23, 24, 25,

26]. Clearly, DNACCs have many interesting applications too, similar to self-assembling particles in general: They can act as ultra-sensitive biomarkers, detectors, efficient drug- or gene-delivery carriers, catalysts, and (optical) filters [7, 11], to mention a few.

There are several ways to synthesize DNACCs. Many different materials, such as rather hard spheres [27, 28, 29, 30], or soft particles [31, 32, 33] such as droplets [34, 35, 36, 37, 38, 39] have been explored when it comes to the colloidal core. This makes it possible to produce sophisticated self-assembling soft matter, *e.g.*, tunable thermo-reversible gels [40].

The general bonding scheme and the structure of the linkers attached to the DNACCs are summarised in Figure 1.

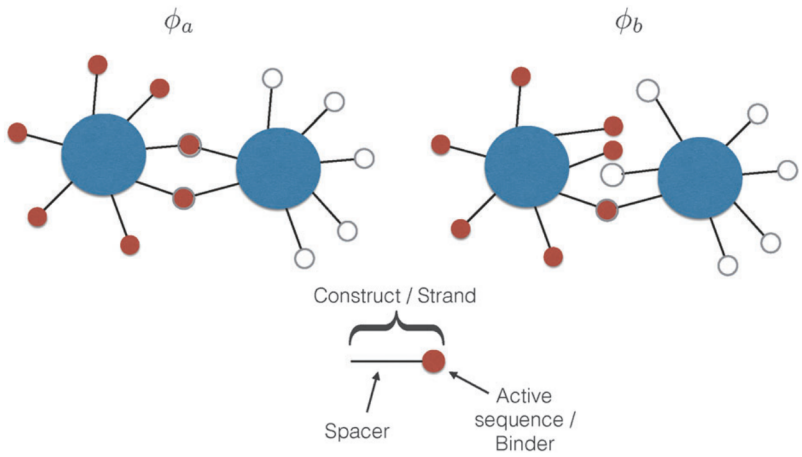

Figure 1: DNACC basic bonding mechanism. Two sets of compatible colloids (red and white) are able to connect to each other via their linkers consisting of spacers made of double-stranded DNA sequences (lines) with sticky ends made of single-stranded DNA sequences (red and white circles). ϕ_a and ϕ_b represent two possible mutually exclusive binding configurations. (Taken from [11])

The single-stranded DNA sequence at the end of each linker can form the aforementioned hybridization bonds with other single-stranded ends from different colloids and thereby connect the particles in the system.

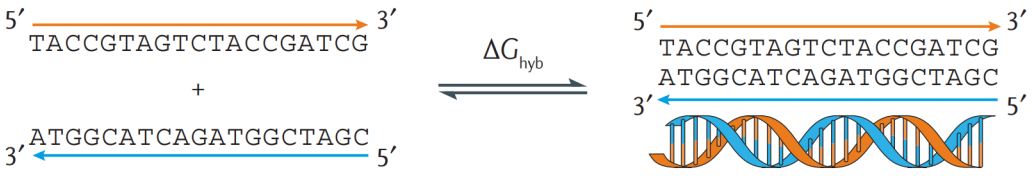

Figure 2: DNA hybridization bonds. Single-stranded DNA sequences are read from the 5' end to the 3' end. Two sequences are compatible if one consists of a base code complementary to the other one, *i.e.*, every C $\mapsto$ G, A $\mapsto$ T, and vice versa. Matching strands are able to connect to each other via hydrogen bonds amongst the base pairs AT (adenine-thymine) and CG (cytosine-guanine). The bonded DNA strands eventually form the typical double helical backbone of a double-stranded DNA sequence. (Taken from [16])

Due to a rather short range of particle interaction compared to the colloid size the particles can get trapped in amorphous aggregates [26, 41, 42]. In order to avoid that scientists thermally controlled the balance of binding/unbinding processes of the DNA linkers [30, 43]. An alternative way to get rid of kinetic traps during self-assembly without breaking the hybridization bonds at any point is to use surface mobile linkers. The ability of the linkers to diffuse along their particles' surface allows for additional binding possibilities within clusters. The bonded particles are able to perform rolling motions, the moving linkers ensure a rather homogeneous linker distribution, and there is no need to turn to binding/unbinding temperature dependant strategies in order to achieve a smooth crystallization process [44, 40, 45]. The mobile linkers also give rise to more control over the valence [46]. The benefits of mobile linkers come with the cost of a higher complexity when it comes to a theoretical understanding of the DNACCs.

When trying to figure out the driving forces within such a complex system, controllable computer simulations play an essential part. Being able to mimic particles and their behaviour while knowing every input parameter allows drawing conclusions on the main dynamics involved. It turns out that knowing every atomistic detail involved in the bonding mechanisms in detail is not essential and sophisticated assumptions result in great virtual DNACC replica [46, 47, 48, 49, 50, 51, 52]. Since complicated systems of DNACCs with mobile surface linkers, specifically their interactions, can not be simulated straightforwardly with atomistic details which would be way too computationally expensive, different coarse-graining methods come into play. Hence, even if the simulated data matches the experiment to some degree, the link between the two oftentimes remains unclear. The main challenge is figuring out the important driving forces involved in the system's dynamics. [11]. What actually is important to know in order to set up a model able to represent accurately the self-assembly dynamics are the relations between the different timescales involved: Typically, at the beginning of the self-assembly process the linkers diffuse on the particle surface with a rate comparable to the Brownian diffusion of the individual colloidal particles in the viscous solvent [53]. However, this ratio changes once the particles find themselves in clustered configurations moving quite slowly compared to the linkers. Additionally, the hybridization of complementary DNA strands in close contact has to overcome electrostatic repulsions and entropic effects, taking a finite characteristic time that also has to be considered. The interplay between these dynamic processes becomes very important for dilute systems, determining the effective valence of the particles.

Most theoretical works [54, 55] focus on the binding/unbinding mechanisms when simulating DNACCs with mobile linkers whereas the role of the kinetics of particle diffusion under stable binding conditions (*i.e.*, at temperatures below T_h) has been barely addressed. The simulations examined in the course of this thesis were performed using the algorithm of Sánchez et al. [56] which was developed to match the recent experiments of McMullen et al. [53] where a

monolayer of colloidal particles with mobile surface linkers at a constant temperature $T < T_h$ has been studied focusing on the self-assembly without breaking the hybridization bonds. The novelty of the algorithm is the ability to mimic stable self-assembly of particles with mobile surface linkers while considering all of the system-defining parameters, paying attention to the different timescales listed above, in a reasonable way. This allows one to look at the system's "end"-configurations after self-assembling for a sufficiently long simulation time under various conditions to actually make use of its tuning ability and eventually map out which consequences certain input variables have on the self-assembly behaviour. Changing the system's DNA-linkers concentration C_{DNA}, the experimentalists were able to observe how the particles formed dimers, freely jointed colloid chains, so-called colloidomers, or networks (cf. Figure 3). Sánchez et al. were not only able to replicate qualitatively the configurations after self-assembling using an analogous linker concentration parameter C_l (see Figure 3 and 4), quantitative agreement with the effective valence measured in experiments (see 5).

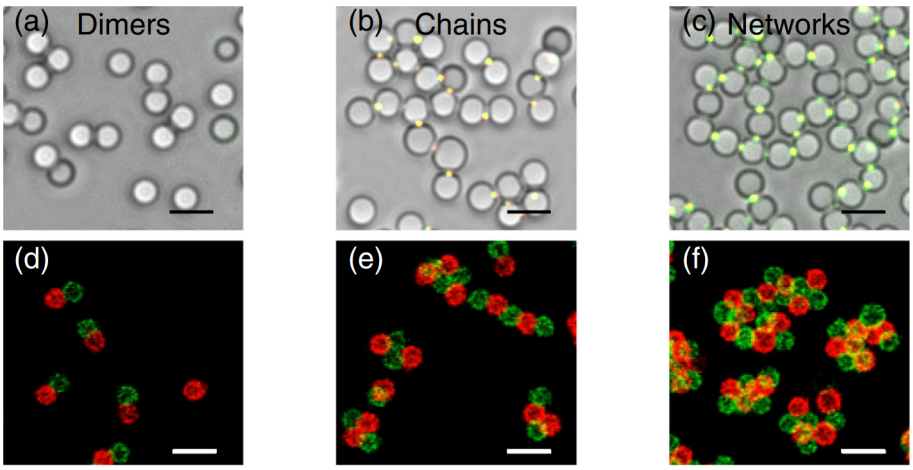

Figure 3: Monolayer of self-assembled DNACCs with different concentrations of DNA polymers involved in the system. The top row displays images from a bright-field microscope and the bottom one contains fluorescence photographs. (Taken from [53])

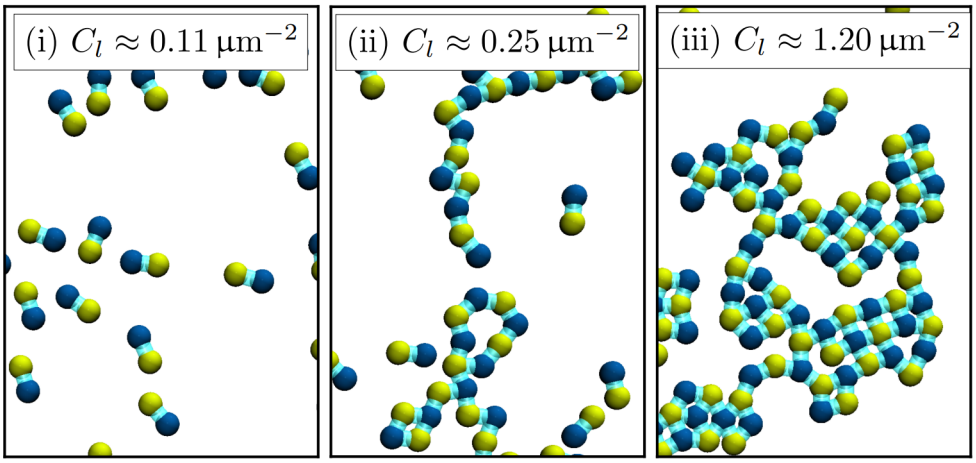

Figure 4: Simulated DNACCs. Depending on the linker concentration C_l the system ends up in different formations: dimers, chains, or clusters. This can also be observed in the experiment by McMullen et al. shown in Figure 3. (Taken from [56])

The structures after the self-assembling process can be classified with the final average coordination number $\langle b \rangle_\infty$, the asymptotic limit of the average number of connections per particle. More details on how to extract this quantity from simulated data can be found in section 4. Figure 5 depicts different results for $\langle b \rangle_\infty$ achieved by [56] when tuning the defining system parameters accordingly (see Table 1 in appendix) corresponding to the kinetically limited effective valence in the experiment [53]: The hybridization time τ_h, the droplet radius R_d, the droplet concentration σ_d, and of course the temperature $T \approx T_{\mathrm{room}} < T_h$ stayed fixed whereas the linker concentration C_l changes just like the concentration of DNA polymers involved in the different experimental setups C_{DNA}. The experiment of McMullen et al. does not provide a measurement of the number of linkers per colloid, the only known quantity is the number of DNA linkers involved when preparing the colloids. Thus, Sánchez et al. had to establish a mapping between the linker concentration used in experiments C_{DNA} and in simulations where every colloid has the same number of linkers ($C_l = N_l/(4\pi R_d^2)$). Assuming a direct proportionality they performed a least squares minimization of the differences between the values for $\langle b \rangle_\infty$ obtained in experiment and simulation. The simulated data has been fitted, shown as the dashed line in Figure 5, to a polynomial of 6th order while the experimental data was weighted emphasizing higher values of $\langle b \rangle_\infty$. The simulated results with lower linker concentrations differ slightly more from the experiment since it is statistically more unlikely to synthesize a monodisperse system, similar to the ideal simulation conditions, where every particle possesses the same number of linkers, with very few linkers involved. It is therefore reasonable to focus on high linker concentrations when quantitatively comparing the two which eventually results in the relationship $C_{\mathrm{DNA}} = 1.2 \cdot C_l$. The mapping procedure is used once for a direct comparison and does not affect qualitatively future results obtained when exploring the parameter space of the kinetically limited DNACC

system with different input parameters. When plotting the value of $\langle b \rangle_\infty$ defining the different "end"-configurations against the changing parameter C_l, respectively C_{DNA}, the quantitative agreement between simulated and experimental results is revealed.

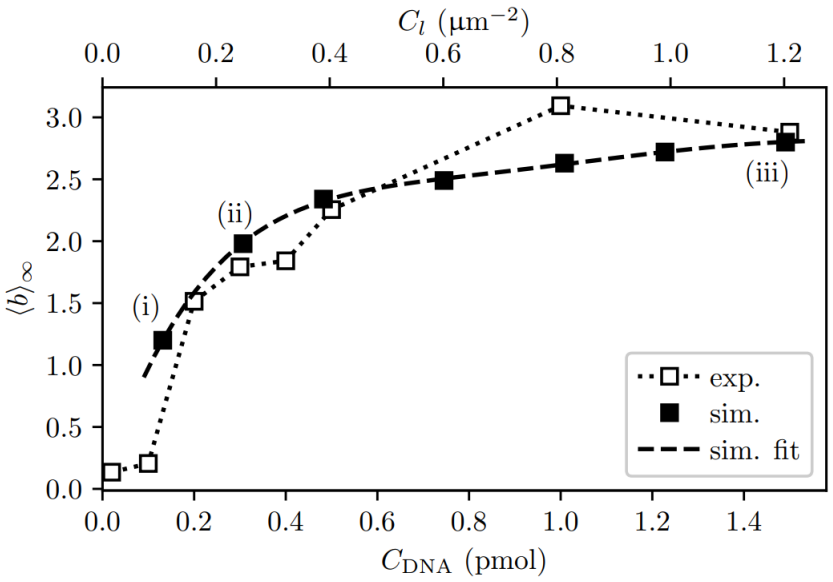

Figure 5: Effective valence $\langle b \rangle_\infty$ experiment vs. simulations. The dotted line serves as a guide for the eye connecting the experimental findings represented by the empty boxes plotted against C_{DNA}. The filled boxes show the results obtained with simulations for different linker concentrations C_l where the ratio between the two concentrations for each data point is given by: $C_{\mathrm{DNA}} \approx 1.2 \cdot C_l$ which is evident by the scales. A least squares fit of a 6th-order polynomial connects the simulation points with a dashed line. (Taken from [56])

The advantage of simulations over experiments would be that each parameter involved in the dynamics can be changed easily. Besides the solvent properties this system, in particular, is determined by the number of linkers attached to each particle (the linker concentration C_l), the value of the different timescales involved in the dynamics, the particle density σ_d and the particle size compared to the linker length. How these parameters influence the overall dynamics of the system will become clear in the next sections explaining the system and its computational model in detail. The aim of this thesis is to study the system self-assembly when changing not only the number of linkers attached to the particles but also using different particle area concentrations, thus providing a theoretical prediction of the configurational phase space beyond available experimental data. The interplay between the two main parameters determining the structures formed under kinetically limited self-assembly conditions will be characterized.

2 System Description and Main Dynamic Processes

As mentioned in the former section, this thesis studies the simplest self-assembling system, a monolayer, consisting of soft-core particles suspended in a solvent-filled box. A semi-flexible double-stranded DNA (ds-DNA) sequence of length d_{ds} with single-stranded DNA (ss-DNA) sequence of length d_{ss} at the end form mobile linkers diffusing on the particle surface due to a mobile anchor on a fluid interface represented by violet circles in Figure 6b. As already mentioned, the mobile linkers allow for more flexibility and less trapped configurations even at a constant temperature $T < T_h$ where the established bonds never break. In the monodisperse, symmetric binary suspension each particle has the same limited amount of linkers attached to the surface. Half of the particles possess solely linkers with ss-DNA sequences A whereas the other half is equipped with linkers that end with A'. The two different single-stranded sequences are complementary in the sense that once they meet, together they can form a double-strand AA', *i.e.*, a hybridization bond, shown in Figure 6b. As mentioned above, the hybridization process takes statistically a finite characteristic time, τ_h. After binding, the linkers stay mobile and can still slide on the particle surface, making rolling motions for the bonded particles possible. The sets are otherwise fully equivalent: every particle has the same diameter d_d and every linker has the same length $d_{ds} + d_{ss}$ (shown in Figures 6b, 12) which is very small compared to the particle size. This results in earlier noted different timescales involved in the dynamics of the system.

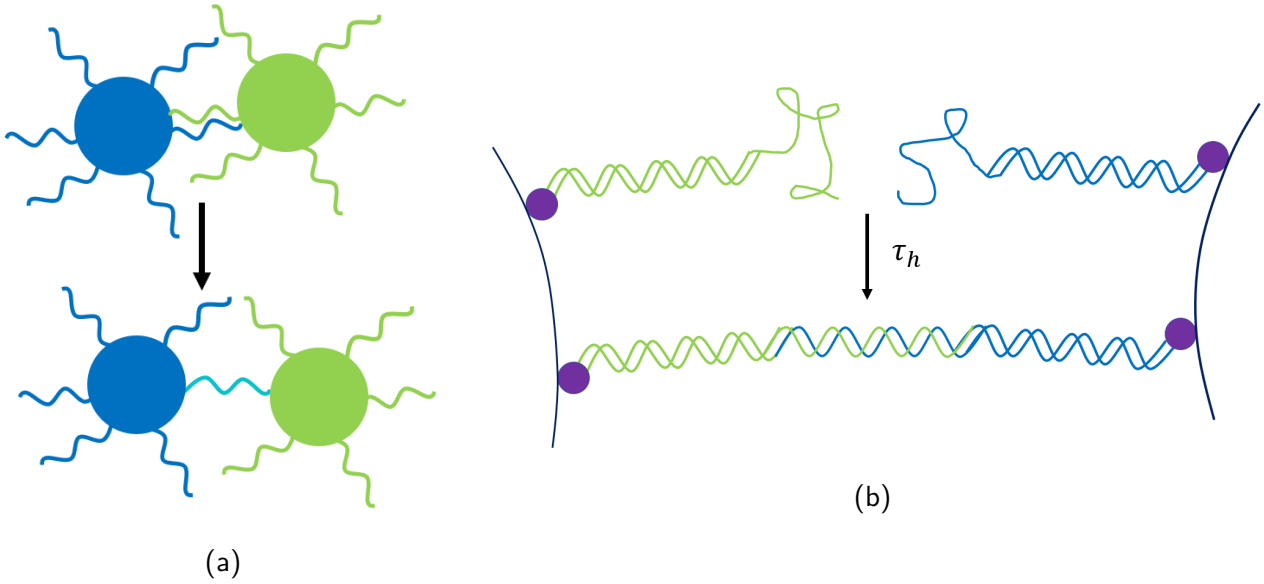

Figure 6: (a) Schematic sketch of two particles meeting and eventually forming a bond. Once the particles remain close for long enough (τ_h), a crosslinker (turquoise line) connecting them can be formed. (b) Close-up of the bonding mechanism: two particles connected by one bond, about to form another one. The linkers are attached to the particles via a mobile anchor (violet circle). The free lines at the end of the double-stranded helices (ds-DNA of length d_{ds}) resemble the bondable ss-DNA with length d_{ss} in blue (A) and green (A'). The lower two linkers have formed one crosslinker, *i.e.*, a hybridization bond AA'.

The time τ_d, illustrated in Figure 7a, refers to the average time it takes for two potential bonding partners to meet, it mainly depends on the diffusion rate and concentration of the particles, thus it tends to increase once slowly diffusing clusters have formed towards the end of the self-assembly process. The free linkers are assumed to diffuse on the particle's surface at a constant rate, defining a characteristic time required to explore the latter, τ_l. Once two particles are close enough for their free linkers to get into close contact, their binding may take place. For this, the particles have to keep such proximity for the characteristic time required by DNA hybridization, τ_h. If hybridization of one pair of complementary linkers takes place, a crosslinker of length $d_l = 2d_{ds} + d_{ss}$ (cf. Figure 6a) is formed and the particles remain permanently connected. From that point on, additional linkers can be recruited from the two newly connected colloids creating more crosslinkers that tend to group into dense regions, forming so-called bonding patches. Thus, these bonding patches grow in time up to a certain geometrical limit when the hybridization region is fully covered in crosslinkers and it becomes impossible to establish new ones (see Figure 9a). On the other hand, remaining free linkers can form crosslinkers with other complementary approaching particles, forming new connections. Figure 8 illustrates these two alternatives for the formation of crosslinkers Figure 7b depicts that a free linker, therefore, only remains free statistically for a certain amount of time τ_l before being trapped into an existing patch.

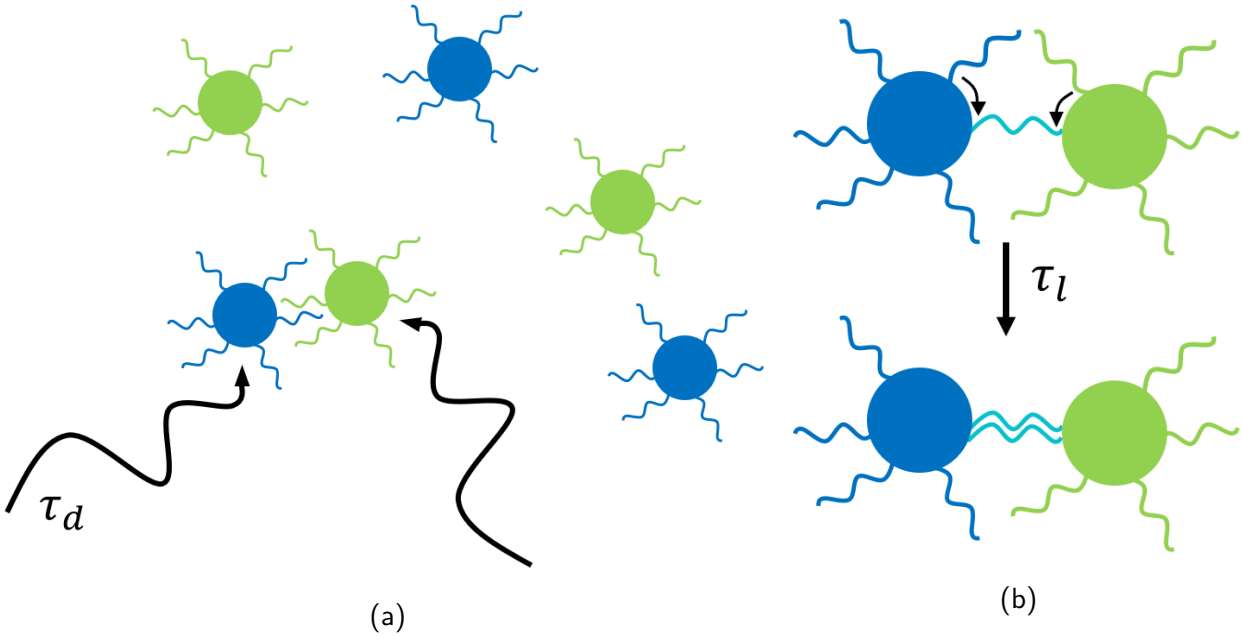

Figure 7: (a) Particle diffusion. The time it takes for two (compatible) particles to meet is determined by their characteristic diffusion time τ_d and therefore their diffusion coefficient D_d. (b) Free linker lifetime. On average, a free linker on a particle that has already formed a patch with another particle stays free for a specific time τ_l until it gets drawn into that patch and forms another bond/crosslinker.

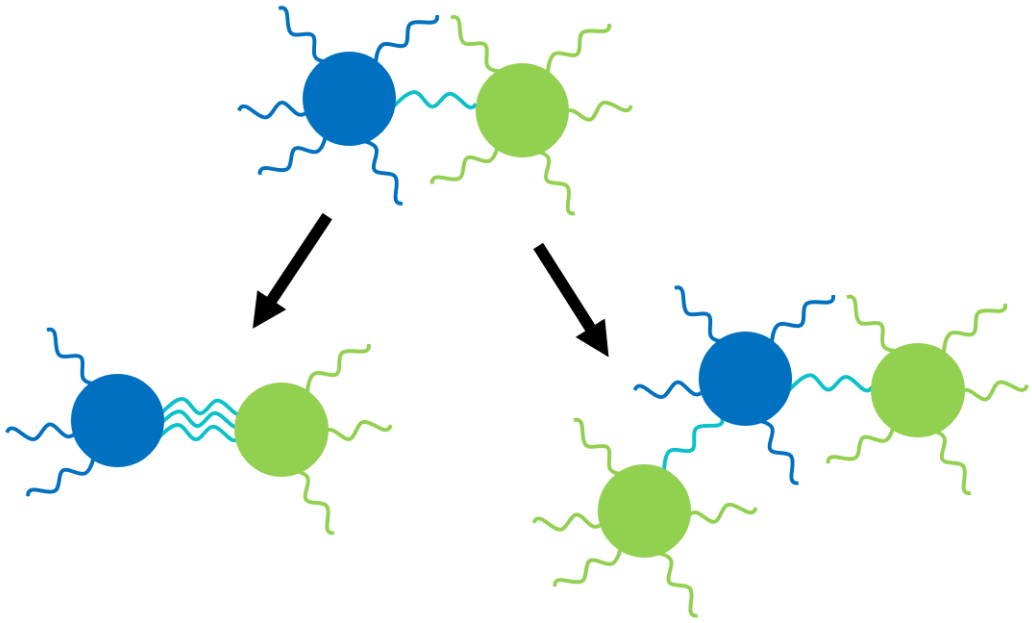

Figure 8: Two competing mechanisms to form crosslinkers. Free linkers can either be recruited by an existing patch or they can create new patches by bonding with different particles.

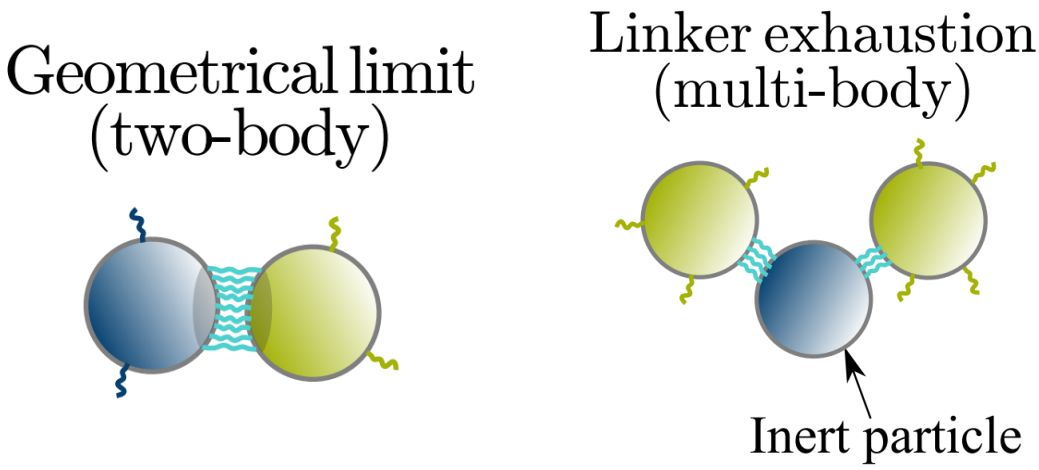

(a) (b)

Figure 9: Two possible saturation scenarios for the growth of the bonding patches due to two competing mechanisms. Picture (a) shows the geometrical limit of the linker recruiting process where a patch reached its maximum size because the crosslinkers occupy the hybridization area entirely. Whereas illustration (b) depicts a particle running out of linkers due to multi-body (more than one bonding partner requesting linkers for the respected patch) effects and eventually becoming inert. (Taken from [56])

In summary, three different timescales determine the assembling dynamics of the particles, and there are two ways a free linker can be used, both illustrated in Figure 8. While τ_l and τ_h stay approximately fixed for the duration of the self-assembly process, τ_d, the characteristic time between collisions of possible bonding candidates, drastically increases once clustered configurations have formed which results in the following relations: $\tau_d \gtrsim \tau_l > \tau_h$ at the beginning, and $\tau_d \gg \tau_l > \tau_h$ at later times.

3 Modelling DNACCs in Suspension

The differences in time scales explained in the previous sections demand restricting the explicit representation of the dynamics to the slowest processes only, that is, to the thermal diffusion of particles and especially clusters, whereas the faster processes involved in the bonding dynamics require a probabilistic implicit description in order to in order to reach experimental time scales. This section will firstly explain how the diffusion dynamics of N explicit colloidal particles in suspension is simulated by means of Langevin dynamics (LD) in the NVT-ensemble. Second, the implicit representation of the bonding dynamics will be described in detail.

3.1 Explicit Part: Particle Diffusion

As mentioned above, the only part of the dynamics that allows an explicit representation in order to reach the long experimental time scales [53] is the thermal diffusion of the relatively large colloidal particles. The latter are considered point particles, avoiding any atomistic details, whose diffusion dynamics follow the Langevin equation. This corresponds to the Newton equations of motion with the addition of a stochastic and a friction term that represent the thermal fluctuations and viscous effects of the solvent. Thus, the velocity and position of each particle i obeys the following equations:

$$\begin{aligned}\vec{v}_i(t+\frac{\delta t}{2}) &= \vec{v}_i(t) + \frac{\vec{F}_i(\{\vec{r}_j(t)\}, \vec{v}_i(t-\frac{\delta t}{2}), t)}{m_d} \\ &= \vec{v}_i(t) + \frac{\delta t}{2}\frac{-\vec{\nabla}_{\vec{r}_i}U(\{\vec{r}_j(t)\}) - \Gamma_T\vec{v}_i(t-\frac{\delta t}{2}) + \sqrt{2k_BT\Gamma_T}\hat{\xi}_i(t-\frac{\delta t}{2})}{m_d}\end{aligned} \tag{1a}$$

$$\vec{r}_i(t+\delta t) = \vec{r}_i(t) + \delta t \cdot \vec{v}_i(t+\frac{\delta t}{2}) \tag{1b}$$

$$\vec{F}_i(\{\vec{r}_j(t+\frac{\delta t}{2})\}, \vec{v}_i(t), t+\frac{\delta t}{2}) = -\vec{\nabla}_{\vec{r}_i}U(\{\vec{r}_j(t+\delta t)\}) - \Gamma_T\vec{v}_i(t) + \sqrt{2k_BT\Gamma_T}\hat{\xi}_i(t) \tag{1c}$$

$$\vec{v}_i(t+\delta t) = \vec{v}_i(t+\frac{\delta t}{2}) + \frac{\delta t}{2}\frac{\vec{F}_i(t+\delta t)}{m_d}. \tag{1d}$$

These equations are integrated by discretizing them in time. The most common integration method, used in this thesis, is the velocity Verlet algorithm [57, Ch. 3.2, p. 97-106] [58], which can be described by the following scheme [59]: Every particle starts out with a certain position $\vec{r}_i(t)$ and velocity $\vec{v}_i(t)$. Equation 1a calculates the velocity (for each particle) at time $t+\frac{\delta t}{2}$ using the current one as well as the acceleration, resulting from the current forces acting on particle i at time t. The final force acting on a particle i depends on three components. $\vec{F}_i(\{\vec{r}_j\})$ represents the deterministic interaction contributions from the other particles j. The term $\Gamma_T\vec{v}_i(t) = k_BT/D$

with the temperature-specific friction constant $\Gamma_T = 6\pi\eta R_d$, following Stokes-Einstein equation and related to the diffusion coefficient of a particle $D_d = k_B T/(6\pi\eta R_d)$, determines friction between particle and solvent. T is the system's temperature, k_B denotes the Boltzmann-constant, η is the viscosity of the fluid, and as mentioned before, R_d is the radius of a particle. The explicit values used are listed in the appendix in Table 1. The stochastic force part $\sqrt{2k_B T\Gamma_T}\hat{\xi}_i(t)$, representing the thermal fluctuations, fulfills the usual fluctuation-dissipation rules:

$$\begin{aligned} &\langle \xi(t) \rangle = 0, \\ &\langle \xi_i^\alpha(t)\xi_j^\beta(t') \rangle = \delta_{ij}\delta_{\alpha\beta}\delta(t-t') \end{aligned} \tag{2}$$

Here, the angled brackets denote an ensemble average, the Greek indices stand for spatial coordinates, and the Latin indices again refer to the different particles, showing that the random pushes from the solvent are completely uncorrelated. Therefore, not only an approximately constant system temperature is guaranteed but simultaneously stochastic processes, *i.e.,* thermal fluctuations from the solvent acting as a heat bath, are included. The random unitary vector $\hat{\xi}_i(t)$ is generated by drawing a random number $\bar{\xi}$ for each spatial coordinate of every particle from a uniform distribution such that: $\langle\bar{\xi}\rangle = 0$ and $\langle\bar{\xi}\bar{\xi}\rangle = 1/\delta t$. It is worth mentioning that this method coarse-grains the system to the point where no particle-particle interaction via the solvent, *i.e.*, hydrodynamic interaction (HI), is included. However, this effect can be neglected because this system is considered to be in thermal equilibrium in a quiescent solvent, so that random kicks sufficiently describe the effects of solvent molecules. The next equation 1b of the integration scheme describes how the new particle positions are calculated with the velocities gained from the previous step. The new forces (eq. 1c) are evaluated in order to update the velocities again by half a time step (equ. 1d). The new positions $\vec{r}_i(t+\delta t)$ and velocities $\vec{v}_i(t+\delta t)$ gained can finally be used to repeat this scheme and eventually achieve well-approximated (discrete) particle trajectories.

The potential and therefore the forces (equ. 1c) used to determine the excluded volume interaction amongst the particles is the pairwise additive Weeks-Chandler-Andersen-potential (WCA-potential) [60]:

$$U_{\mathrm{WCA}}(r_{ij}) = \begin{cases} 4\epsilon_s \left[\left(\frac{\sigma}{r_{ij}}\right)^{12} - \left(\frac{\sigma}{r_{ij}}\right)^{6} + \frac{1}{4}\right] = U_{\mathrm{LJ}}(r_{ij}) - U_{\mathrm{LJ}}(r_{\mathrm{cutoff}}), & r_{ij} < r_{\mathrm{cutoff}} \\ 0, & r_{ij} \geq r_{\mathrm{cutoff}} \end{cases} \tag{3}$$

It defines an excluded volume $\frac{4}{3}\sigma^3$ for a particle i related to its diameter $d_d = 2 \cdot R_d = \sigma$ which results in a soft (also [61]) repulsion between the particles i and j that are $r_{ij} = |r_i - r_j|$ apart. The cutoff radius $r_{\mathrm{cutoff}} = \sqrt[6]{2}\sigma$ is chosen such that the potential 3 is purely repulsive and continuously differentiable. The potential's strength and therefore the energy scale for each

particle is determined by $\epsilon_s > 0$. The WCA-potential represents an amendment of the Lennard-Jones-potential that mimics the characteristic Van-der-Waals attraction ($\propto -1/r_{ij}^6$) between particles at larger distances and a repulsive, empirically estimated term due to the Pauli exclusion principle for short-range interactions ($\propto 1/r_{ij}^{12}$):

$$U_{\mathrm{LJ}}(r_{ij}) = 4\epsilon_s \left[\left(\frac{\sigma}{r_{ij}} \right)^{12} - \left(\frac{\sigma}{r_{ij}} \right)^{6} \right]. \tag{4}$$

Each atom in particle i has a quantum mechanical dipole that approximately acts on each atom in particle j with a potential $\propto 1/r_{ij}^3$ (and vice versa). Integrating over the particles' volumes gives the overall typical Lennard-Jones-interaction $\propto -1/r_{ij}^6$ even for the classical limit. Since long-range interactions are not of interest and can be neglected in a good solvent, the WCA-potential sufficiently provides a representation of soft-core particles focusing on their repulsive interactions. Figure 10 compares the two potentials in a dimensionless plot.

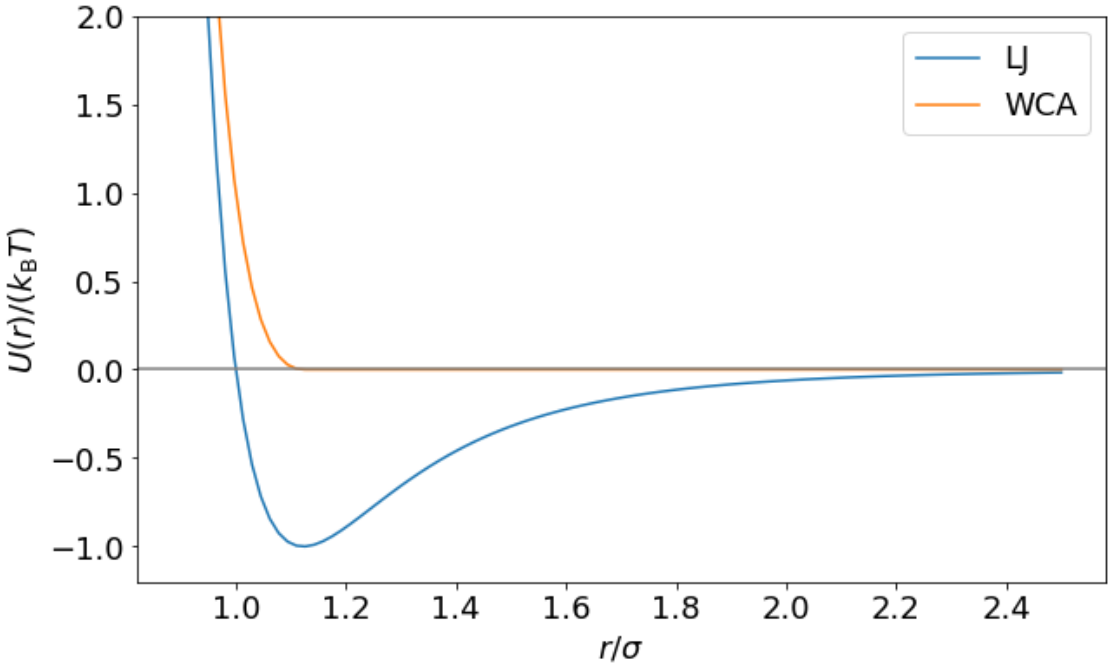

Figure 10: Lennard-Jones-potential vs. WCA-potential.

In this experiment, the particles move right underneath the box cover due to their buoyancy. In order to avoid noteworthy finite-size effects, a pseudo-infinite system is simulated by using lateral periodic boundaries. The simulation box lengths in the direction of the periodic boundaries, that is, in x- and y-direction, are the same $l_x = l_y = (N\pi R_d/\sigma_d)^{1/2}$ and depend on the desired particle area concentration σ_d for a fixed number of particles N whereas the small box length in z-direction remains fixed $l_z = 3d_d = 6R_d$ and the particles are only able to move in lateral directions.

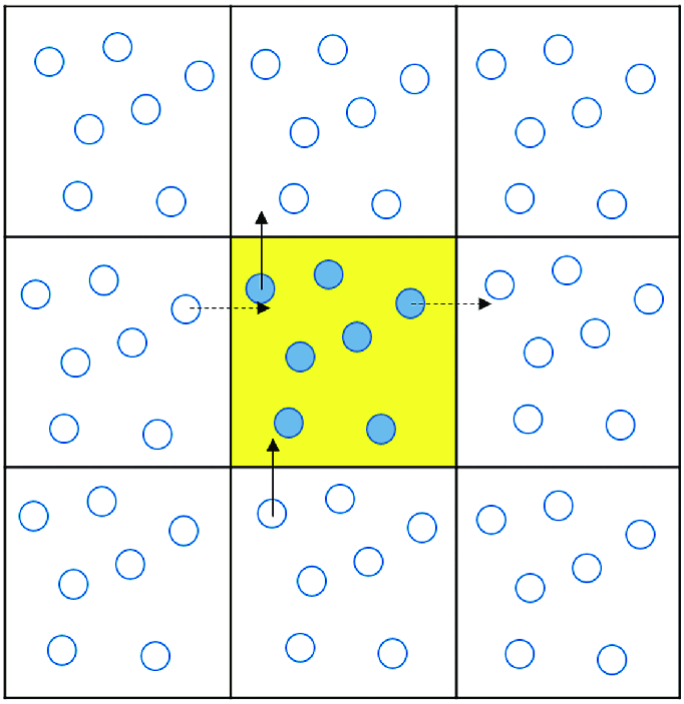

Figure 11: Lateral periodic boundary conditions. The coloured box in the middle represents the actual simulation box. Its periodic replicas allow a particle to leave the box on one side and enter it again on the opposite side which is visualized with arrows. (Taken from [62])

As shown in figure 11, whenever an LD step causes a particle to leave the box in dimension α: $r_i^\alpha(t+\delta t) < 0$ or $> l_\alpha$, it enters the box from the opposite side again: $r_i^\alpha(t+\delta t) \mapsto r_i^\alpha(t+\delta t) \pm l_\alpha$.

Before even running the actual simulation and measuring the particle trajectories, the system must be in a starting configuration with reasonable energy. After initializing the particles at random positions in the box, a relaxation period must take place in order to avoid particles overlapping. Therefore, the overall force calculated in equations 1a and 1c is constrained to a maximum cut-off so that configurations with high potential energy, *i.e.*, very close or even overlapping particles, can be removed gradually without particles flying nonphysically through the system due to too strong forces. After a certain amount of LD steps, once any significant overlap is removed and the system's potential energy is low enough the artificial constraint on the forces is removed and the simulation of the actual system dynamics is started.

3.2 Implicit Part: Bonding Dynamics

Considering the explicit simulation of the thermal diffusion of the particles, it would be unreasonable to also model the dynamics of the linker-DNA-polymers, containing numerous monomers, explicitly. Their dynamics are much faster compared to the droplets since they are also much smaller. The monomers would require a very small integration time step making it computationally unfeasible to reach meaningful simulation times. Hence, as mentioned above, particle bonding

is realized implicitly. So, whenever two compatible particles (i with A-linkers, and respectively j with A'-linkers) get close to each other, *i.e.*, a certain cutoff-distance apart (center-to-center-distance $d_{cc} < 2R_d + d_l$, see Figure 12), within one LD step they become potential bonding partners and will be book kepts as such. Next, the probability for these two particles to actually form their first bond/connection is estimated taking into account the homogeneous distribution of linkers due to surface diffusion:

$$P_{i,j} = \min\left(n_{l,i}(t)\frac{S_h^0}{S_{\text{free},i}(t)},\, n_{l,j}(t)\frac{S_h^0}{S_{\text{free},j}(t)}\right)\cdot(1-e^{-\delta t/\tau_h}). \tag{5}$$

The LD time step is again denoted by δt, and together with the hybridization time τ_h the exponential term represents an attempt rate for a stochastic process with a given characteristic time. The number of free linkers diffusing on the surface of particles i and j are $n_{l,i}(t)$, respectively $n_{l,j}(t)$. At the beginning of every simulation all particles have the same number of free linkers, $n_{l,i}(t=0) = n_{l,j}(t=0) = n_l^0 = C_l 4\pi R_d^2$, determined by the linker concentration determined by the linker concentration C_l. However, this number tends to decrease in time as crosslinkers are formed. S_h^0 stands for the initial hybridization area, *i.e.*, the surface area on the particle of interest on which the first bond/crosslinker connecting those two particles is able to form. It is bound by the length of a stretched crosslinker d_l consisting of two bonded linkers, as well as the center-to-center distance d_{cc}, pictured in Figure 12. Strictly speaking, the hybridization area the hybridization area $S_h(t)$ decreases over time once more crosslinkers connect the particles and the patch size $S_p(t) = S_h^0 - S_h(t)$, shown in Figure 12a, grows.

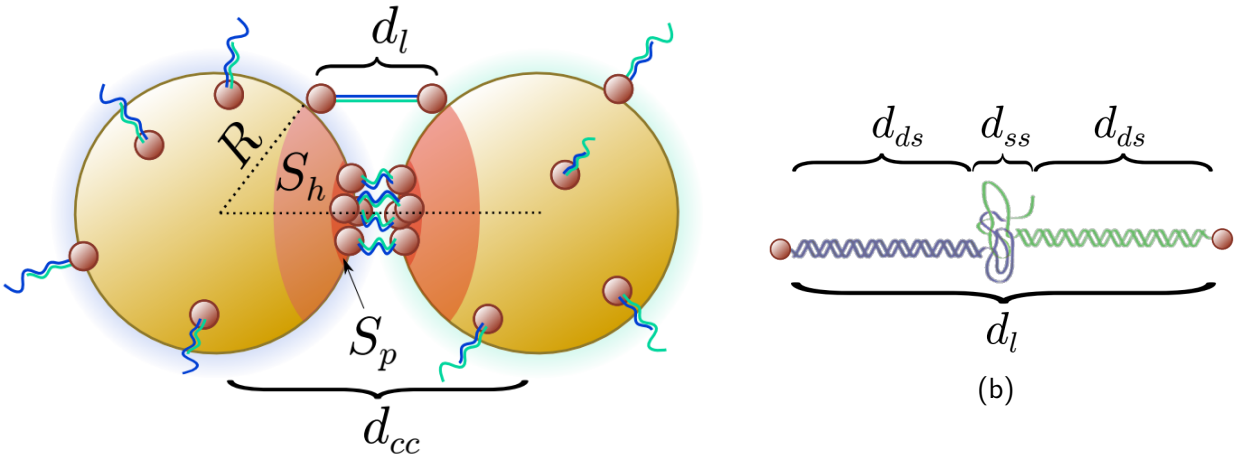

(a) (b)

Figure 12: Geometry of two bonded particles with radius $R = R_d$. $S_h = S_h(t)$ denotes the area where the hybridization of two strands can still happen, while $S_p = S_p(t)$ is the area occupied by already formed crosslinkers which are assumed to group in the central region of S_h (a). The area providing the possibility of bonds forming $S_h(t) = S_h(0) - S_p(t) = S_h^0 - S_p(t) \approx \pi R_d(2R_d + d_l - d_{cc}) - S_p(t)$ decreases over time once more and more crosslinkers occupy the surface by $S_p(t)$. The length of a maximum stretched crosslinker $d_l = 2d_{ds} + d_{ss} = 2n_{ds}s_{ds} + n_{ss}s_{ss}$ is defined by the extension of the double-stranded DNA linkers (n_{ds} parts with length s_{ds}) as well as the length of their parallel aligned single-stranded sticky ends (respectively, n_{ss} parts with length s_{ss}) (b). (Taken from [56])

However, this time dependence can be ignored thanks to the following considerations. Despite their soft nature, the particles hardly show deformation in experiments [61] [37] and can therefore be thought of as spheres which makes the hybridization region S_h^0 a spherical cap with surface area $A = 2\pi r \cdot h = 2\pi R_d \cdot (d_l - d_{cc} + 2R_d)/2$ (cf. Figure 13). The fluctuating particle distance $d_{cc} = d_{cc}(t)$ technically makes S_h^0 a time dependent quantity with values ranging from 0 ($d_{cc} = 2R_d + d_l$, maximum distance reached for fully stretched crosslinkers) to $\pi R_d d_l$ ($d_{cc} = 2R_d$, minimum distance due to excluded volume). Clearly, above $d_{cc} = 2R_d + d_l$ no bonding is possible:

$$S_h^0 \approx \begin{cases} \pi R_d(2R_d + d_l - d_{cc}), & d_{cc} < 2R_d + d_l \\ 0, & d_{cc} \geqslant 2R_d + d_l \end{cases} \tag{6}$$

In order to sample the different possible configurations $0 \leqslant d_{cc} < 2R_d + d_l$, while making the algorithm not too computationally costly and thus again reaching the important long experimental time scales, S_h^0 can be assumed to amount to a constant average value $\langle S_h^* \rangle \approx \pi R_d d_l$ when choosing the Langevin integration time step δt accordingly big. This is justified under the assumption that the linkers are small compared to the droplet radius $d_l << R_d$ which results in the diffusion time of the droplets τ_d being of significantly bigger scales than the residence time of two possible bonding candidates, *i.e.*, the time period two droplets stay next to each

other $d_{cc} < 2R_d + d_l$. Hence, two completely unbound particles meeting leads to an effective constant initial hybridization region substituting the calculation of equation 6. Details on these considerations can be found in the appendix.

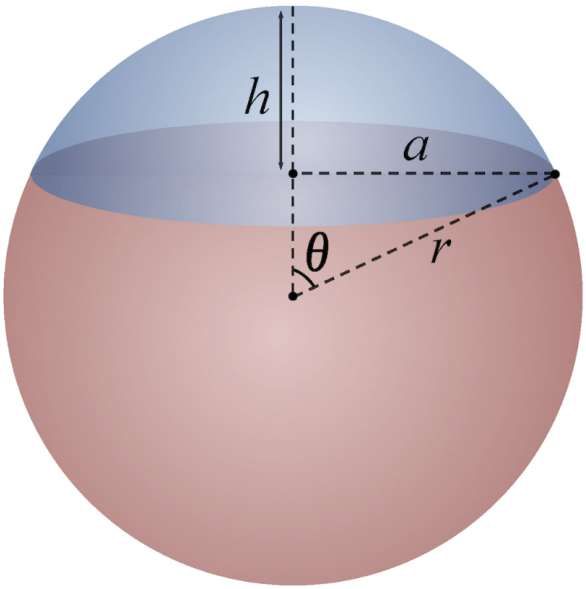

Figure 13: Dimensions of a spherical cap representing the hybridization region S_h^0. The droplet sphere is of size $r = R_d$ and the caps depth amounts to $h = (d_l - d_{cc} + 2R_d)/2$ (Taken from [63])

In conclusion, the first term of equation 5 represents the average number of free linkers belonging to each particle diffusing within the available hybridization region, implying a limitation via the particle with the lower number of free linkers. But whether a bond between two particles will be formed also depends on the duration the particles are close to each other so that there is enough time for hybridization to occur, as represented by the second term.

After calculating the first bonding probability, the result is used to sample whether or not the bond actually forms by drawing a random number from a uniform distribution and then compared to the probability. If this random number is smaller than the value of $P_{i,j}$ the bond is established and stored, otherwise the two particles remain book kept as potential bonding partners as long as they stay close to each other $d_{cc} < 2R_d + d_l$ and will be checked regarding their bonding probability for the next LD steps. Once two particles are chosen to establish their first connection an additional bonding potential is added to the newly connected particles: The finitely extensible nonlinear elastic (FENE) potential [64]:

$$U_{\mathrm{FENE}}(r_{ij}) = -\frac{K_b r_{\max}^2}{2} \ln\left[1 - \left(\frac{r_{ij}}{r_{\max}}\right)^2\right]. \tag{7}$$

$K_b = 3{\cdot}\epsilon_s$ defines the strength of the bonds which has been chosen arbitrarily but significantly high in relation to the strength of the WCA-potential, that way the bonds will not break throughout the

entire simulation. And $r_{\max} = d_l$ is the maximum stretching length of a bond/crosslinker. The potential was originally established to approximate the behaviour of polymer chains. It represents an enhancement of the bead-spring model with harmonic bonding potential by including a limit to the bond extension that avoids too unrealistic stretching, replicating a more rigid structure. Figure 14 displays the plots of the two interaction potentials involved in the simulations as well as the resulting potential a bonded particle eventually feels.

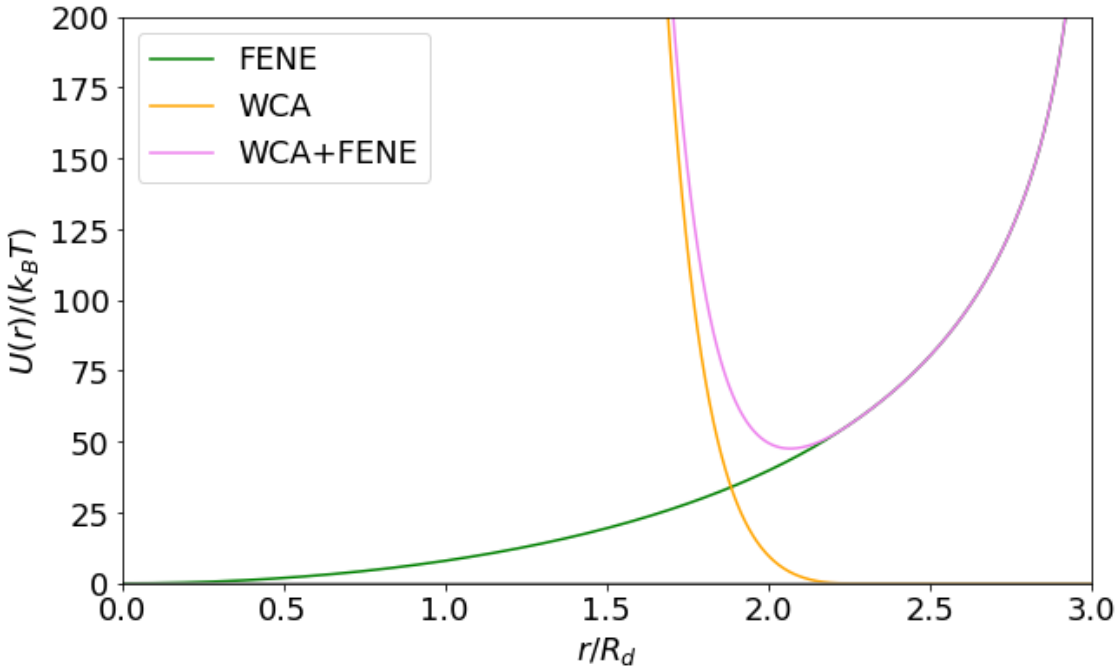

Figure 14: The two interaction potentials and their resulting sum $U_{\mathrm{WCA}} + U_{\mathrm{FENE}}$.

The potential acting on particle i in equations 1a and 1c changes to:

$$U(t + \delta t) = U_{\mathrm{WCA}}(\{\vec{r}_j(t + \delta t)\}) + U_{\mathrm{FENE}}(\{\vec{r}_{j'}(t + \delta t)\}), \tag{8}$$

where j again denotes the particles that are within the WCA cutoff radius and j' would be all the particles bonded to colloid i.

After two particles are connected by one crosslinker, some of their other linkers could form additional first bonds with different particles. The respective probability function (eq. 5) needs to be calculated, where the free surface areas $S_{\mathrm{free},i}$ and $S_{\mathrm{free},i}$ technically (further details below) have been decreased by the patch area.

At the same time, the original patch between the particles i and j can also grow due to more and more linkers being recruited into the first bond. The patch growth rate is again realized implicitly assuming that it is mainly determined by the diffusion of the linkers with diffusion coefficient D_l. The number of crosslinkers within the patch of interest (original particle i and j) $n_c(t)$ at time t is therefore expected to grow from its initial value $n_c(t_0)$ (result of eq. 5)

with the previously mentioned characteristic rate τ_l and saturate to a certain maximum value n_c^{sat}. A simple saturation model for the recruiting process can be assumed, given by the following differential equation

$$\begin{aligned} &\tfrac{dn_c(t)}{dt} = \tau_l^{-1}\left[n_c^{\mathrm{sat}} - n_c(t)\right] \\ &\longrightarrow n_c(t) = n_c^{\mathrm{sat}}(t) + \left[n_c(t_0) - n_c^{\mathrm{sat}}(t)\right] e^{-t/\tau_l}. \end{aligned} \tag{9}$$

This linker lifetime is given by:

$$\tau_l \approx \log_{10}\left[\frac{1}{1.55}\left(\frac{2R_d + d_l - d_{cc}(t)}{R_d}\right)^{-2.26}\right]\frac{R_d^2}{D_l}. \tag{10}$$

The formula involves the particle size R_d the crosslinker length d_l, the center-to-center distance of the two already connected particles, and the diffusion constant of the linkers moving around the particle surface D_l. A detailed derivation of equation 10 can be found in the appendix. The saturated number of connections between particles i and j is generally (before certain additional assumptions) given by:

$$n_c^{\mathrm{sat}}(t) = \min(n_c(t) + \min(n_{l,i}(t), n_{l,j}(t)), n_c^{\mathbf{max}}). \tag{11}$$

Again, $n_{l,i}(t)$ and $n_{l,j}(t)$ denote the number of free linkers on the respective particle, and $n_c^{\max}$ is the maximum number of crosslinkers possible regarding the geometrical limit of the patch size $S_p(t) \lesssim S_h^0$, *i.e.* how many crosslinkers are able to fit in the patch which can be assumed remain constant with a characteristic size due to the rather rigid nature of the particles [61]. However, the different numbers of linkers used in the simulations done in the course of this thesis are chosen low enough such that: $n_{l,i}(t)$, $n_{l,j}(t) < n_c^{\max}$ which leads to the modification of equation 11 $n_c^{\mathrm{sat}} \approx n_c(t) + \min(n_{l,i}(t), n_{l,j}(t))$. Hence, the geometrical limit will not have any impact, and the hybridization region $S_h(t) \approx S_h^0$ can be assumed to not decrease because of the patch growth since $S_p(t)$ stays small. This allows for the free surface areas $S_{\mathrm{free},i} = S_{\mathrm{free},j} \approx 4\pi R_d^2$ in equation 5 to correspond to the entire surface area of a particle throughout the simulation. The equations 11 and 9 are not discretized and all the time dependant amounts of linkers involved are considered to be non-integers. Once the number of free linkers of a particle falls below 1, the recruiting stops and the particle becomes inert (cf. fig 9). The additional bonds only affect the number of free linkers but not the overall bonding potential (equ. 8) used to calculate the forces for each LD step. If one particle has several existing patches the recruited number of linkers for one randomly chosen patch (a fractional value resulting from equations 9 and 11) will be calculated and added to the crosslinkers of that patch while simultaneously subtracted from the number of free linkers. The process will then be repeated for the next patch on that particle, again randomly chosen, until every patch has been dealt with.

Recapitulatory has to be said that, under the conditions of low to moderate concentrations of particles and linkers considered here, the connectivity of the particles is governed by kinetic many-body effects as shown in Figure 9b. The characterization of this kinetically controlled self-assembly regime represents an exciting theoretical challenge that is aimed at being unveiled by the results presented in the following Sections of this thesis.

4 Results and Discussion

The monolayer of a symmetric binary DNACC-mixture (equal parts of A and A') can be in different configurations after saturation, *i.e.*, after most of the particles become inert and hardly any new crosslinkers, will be formed. The particles can end up in certain formations, *e.g*, network clusters, chains, or dimers, depending on the number of patches they were able to form with other particles.

Particle diffusion properties, derived from the particle radius $R_d = 1.5 \cdot 10^{-6}\,\mathrm{m}$, the solvent viscosity and temperature (water at $T \approx T_{\mathrm{room}}$; more details in appendix Table 1) stayed constant for every simulation run, the same is true for the hybridization time $\tau_h = 0.02\,\mathrm{s}$, the linker diffusion constant $D_l = 2 \cdot 10^{-13}\,\mathrm{m}^2/\mathrm{s}$ defining τ_l, and the maximum crosslinker length $d_l << R_d$. The LD time step is chosen such that the algorithm replicates a real particle's trajectory as close as possible, while simultaneously keeping the simulation feasible in terms of speed and efficiency. [57, Ch. 3.2, p. 98] Here, $\delta t = 5 \cdot 10^{-7}\,s$ which is small enough to ensure a precise particle trajectory because the integration time step is significantly smaller than the time it takes for a particle to move its own size but the system is still able to reach a state of saturation within a reasonable simulation time on the computer.

What has been changed and examined are the particle area concentration σ_d and the linker concentration C_l. The density σ_d can be varied by keeping the number of particles $N = 256$ constant and changing the box length. For simplicity it can be assumed that every particle has the same amount of linkers, therefore, C_l corresponds to the number of linkers per particle divided by its surface area. Every data point created in this thesis has been generated by taking the ensemble average over five independent runs with the exact same parameters.

This section will first explain how to quantify the various "end"-configurations before showing the results for different system parameters and finally show that the two changing concentrations σ_d and C_l not only impact the properties of the system after self-assembling but also the dynamics throughout this process.

4.1 Calculating the Effective Valence: Asymptotic Average Coordination Number

The various possible system configurations during the self-assembly process can be classified by the connectivity of the particles involved which is represented via their average coordination number $\langle b \rangle(t)$, *i.e.*, that is the number of patches one particle on average (considering all the particles in the simulation) has formed at time t. Plotting this quantity against the simulation time in a logarithmic scale reveals a sigmoid-like shape for every parameter set which is typical for systems with limited growth behaviour (cf. Figure 9), as it can be observed in the examples

Figure 15 looking at all the different particle concentrations with a fixed linker concentration ($C_l = 0.4\,\mu\mathrm{m}^{-2}$ for the first plot and $C_l = 1.4\,\mu\mathrm{m}^{-2}$ for the second), and Figure 16 displaying the curves for every linker concentration sampled keeping $\sigma_d = 0.2$, respectively $\sigma_d = 0.6$ fixed.

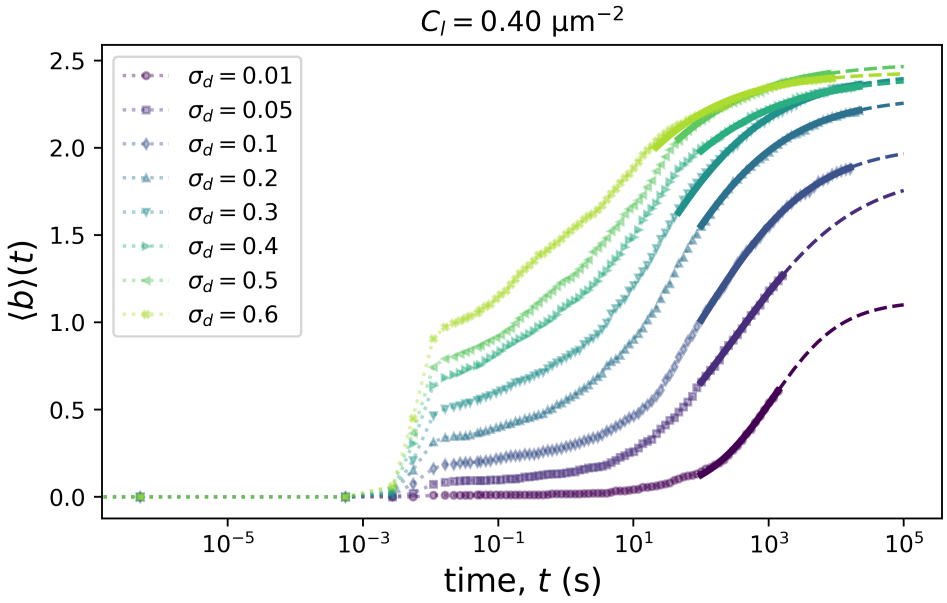

(a)

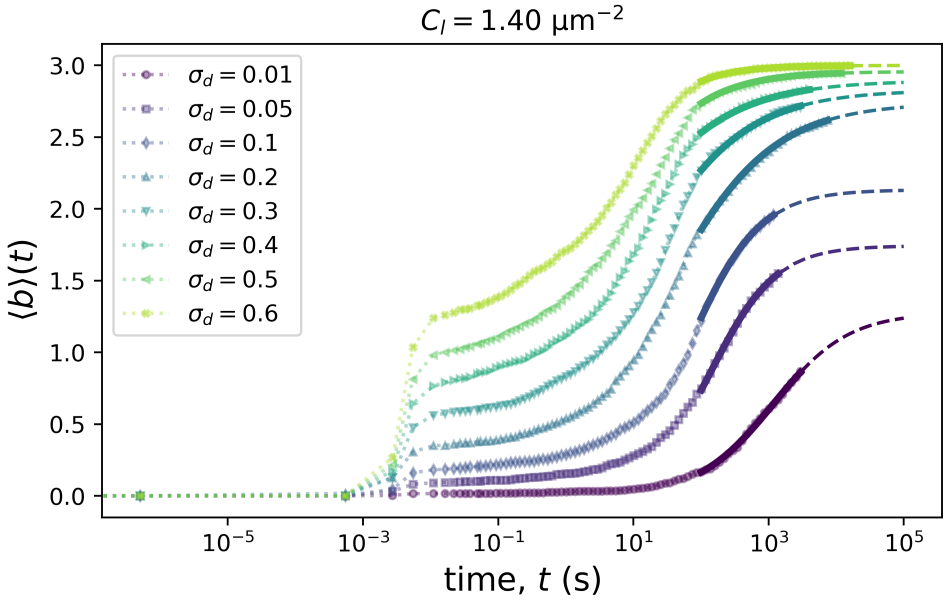

(b)

Figure 15: (a) Average coordination number of systems with different particle concentrations σ_d at fixed $C_l = 0.4\,\mu\mathrm{m}^{-2}$ (a) and $C_l = 1.4\,\mu\mathrm{m}^{-2}$ (b). The curves $\langle b \rangle(t)$ behave sigmoid-like with different asymptotic limits characterized by the fitting parameter $\langle b \rangle_\infty$ and a shifting inflection point t_0 depending on σ_d. The latter could suggest that t_0 is determined by τ_d. However, this effect could not be analyzed in the course of this work. The solid lines represent the fit to equation 12 using the respective data (coloured symbols underneath) whereas the dashed lines are extrapolations of the fitted function.

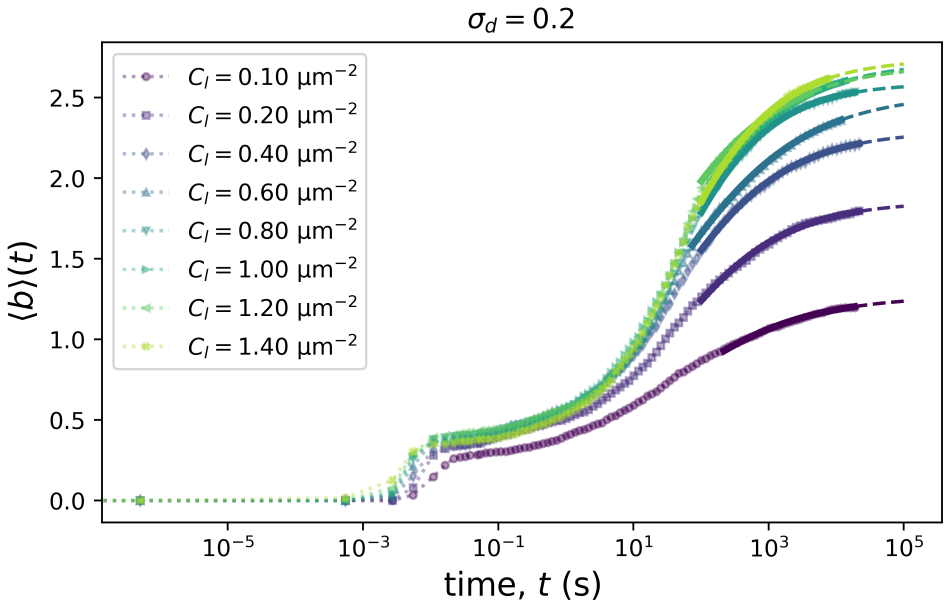

(a)

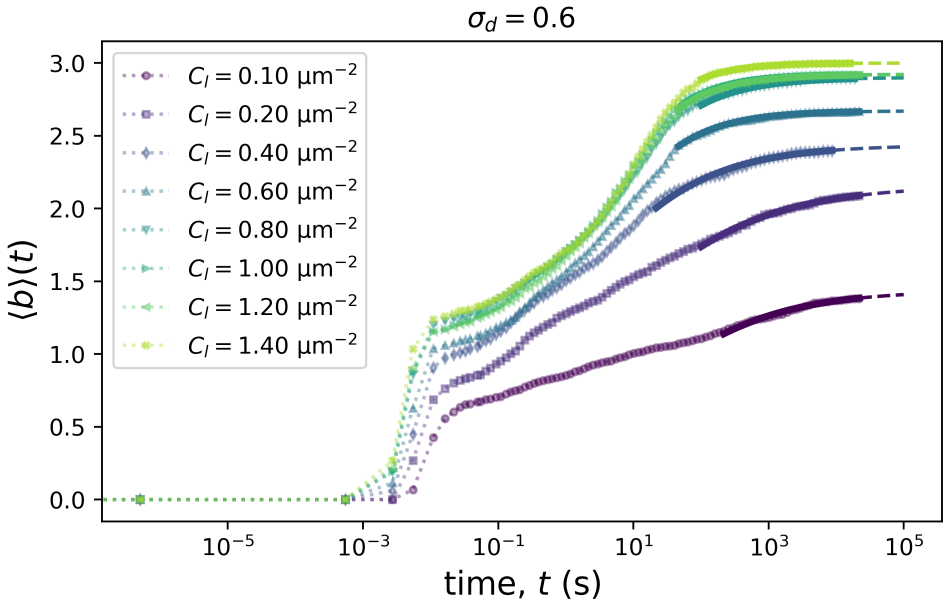

(b)

Figure 16: Average coordination number of systems with different linker concentrations C_l with $\sigma_d = 0.2$ (a) and $\sigma_d = 0.6$ (b). Here, the coinciding inflection points t_0 give another hint that the boundary of the two self-assembly dynamic regimes mainly depends on σ_d rather than on C_l.

In general, the simulations were run up to at least $2 \cdot 10^4\,\mathrm{s}$. In most cases that time was enough to approach the saturation of the self-assembly process, in which most particles become inert and no further connections can be established. At this point, the average coordination number approaches an asymptotic limit $\langle b \rangle_\infty$ which can then be calculated by fitting the simulated data

at later times to a logistic-like function:

$$\langle b\rangle(t\to\infty) = \langle b\rangle_\infty \left(1 - \frac{1}{1+(t/t_0)^p}\right). \tag{12}$$

To examine the approach to the asymptotic limit $\langle b\rangle_\infty$ the data have been weighted (each data point has a weight $\sigma(t) = \sqrt{t_{\max}/t}$ according to its time t with maximum time reached in that simulation run $t_{\max}$) emphasizing the late dynamics. The important value $\langle b\rangle_\infty$ represents the kinetically limited effective valence of the particles and is the simplest parameter characterizing the different self-assembled structures. Thus, this parameter will be used to analyze the dependence of the self-assembled phases on the concentrations of particles and linkers.

4.2 Structural Phase Diagram for Particle and Linker Concentrations

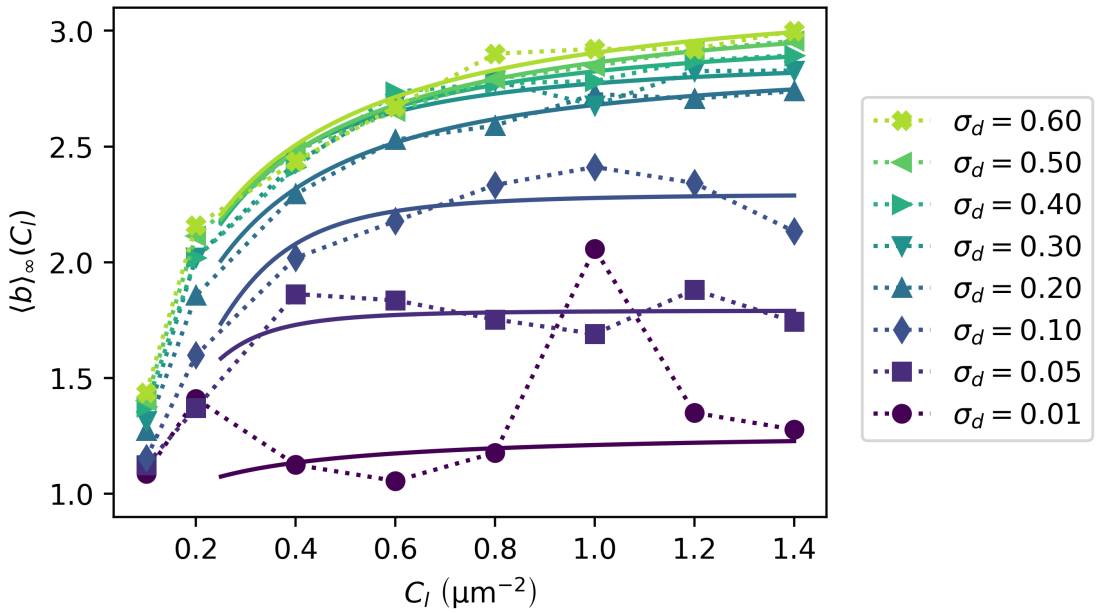

(a)

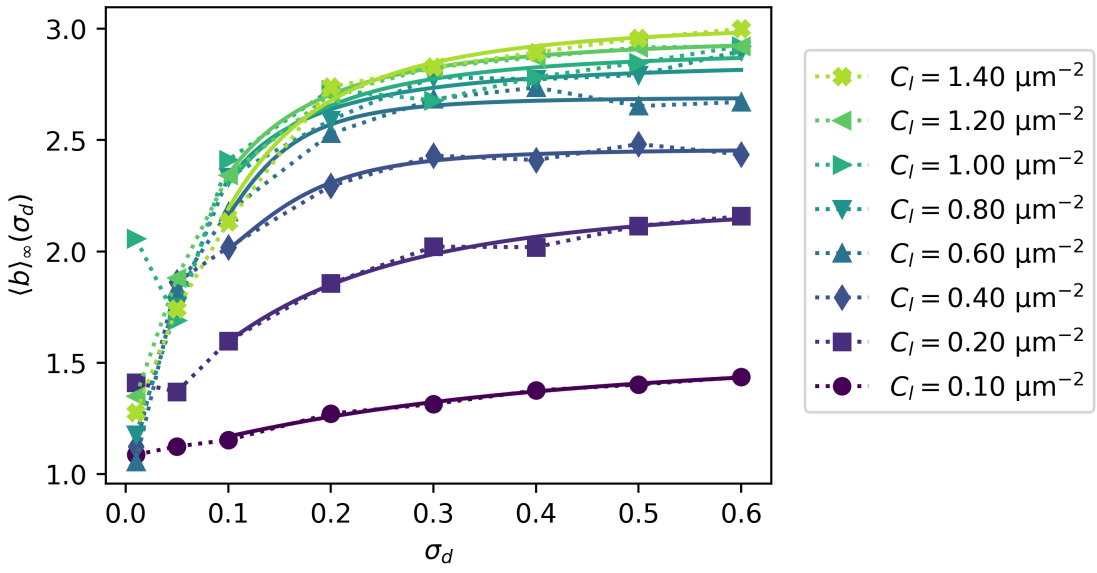

(b)

Figure 17: (a) $\langle b \rangle_\infty(C_l)$ for different particle concentrations σ_d shown with the respected colour and symbol. (b) $\langle b \rangle_\infty(\sigma_d)$. The fits are achieved as described in the main text (equations 13 and 13b) and underline the asymptotic behaviour of each curve with respect to either concentration.

The procedure described above and illustrated in Figures 15a and 16a is now performed for the whole parameter space of interest covering eight different linker concentrations (number of linkers per particle N_l) $C_l \in (0.1, 0.2, 0.4, 0.6, 0.8, 1.0, 1.2, 1.4) \widehat{=} N_l = (3, 6, 11, 17, 23, 28, 34, 40)$ paired with eight particle concentrations $\sigma_d \in (0.01, 0.05, 0.1, 0.2, 0.3, 0.4, 0.5, 0.6)$. For the fitting of

$\langle b \rangle(t)$ the initial guesses for the different parameter sets were chosen carefully looking at each of the resulting 64 plotted data sets individually and deciding on the inflection point t_0 and the asymptotic limit while keeping $p = 0.5$. As mentioned before, the data has also been weighted focusing on the later simulation times. After calculating 8x8 values for $\langle b \rangle_\infty$, the results can then be plotted against C_l or σ_d, both dependencies are shown in Figure 17 also revealing an interestingly revealing what also seems to be a limited growth behavior with both, σ_d and C_l. The resulting values for the parameter sets with the two lowest particle concentrations, especially the very lowest σ_d, need to be taken with a grain of salt since they were not able to approach a saturated enough state in the framework of this thesis. It obviously takes longer to drive a very dilute system to saturation since the singlets do not meet each other for many LD steps. The respective curves are not close enough to saturation in order to sufficiently estimate their asymptote which is apparent by looking at the darkest curve in Figure 15a representing $\sigma_d = 0.01$. In order to prove the qualitatively equivalent limited growth behavior of $\langle b \rangle_\infty$ for σ_d and C_l, the collapse of the results into master curves has to be checked. To minimize the impact on the rescaling factors of the statistical errors, which for low concentrations are rather large, we also fit logistic-like growth curves to the data (solid lines in plots of Figure 17):

$$\langle b \rangle_\infty^{\mathrm{fit}}(C_l) = s_1 \left(1 - \frac{1}{1 + (C_l / C_l^0)^{p_1}} \right) + d_1 \tag{13a}$$

$$\langle b \rangle_\infty^{\mathrm{fit}}(\sigma_d) = s_2 \left(1 - \frac{1}{1 + (C_l / \sigma_d^0)^{p_2}} \right) + d_2 \tag{13b}$$

For this fitting, notorious outliers have been disregarded, the initial guesses for the parameters (cf. eq. 13:$[s_1, C_l^0, p_1, d_1]$ and $[s_2, \sigma_d^0, p_2, d_2]$) were chosen individually, and the weights focus on more accurate values with higher linker/particle concentration in order to achieve reasonable asymptotic curves:

Figure 18 shows the collapse of the data rescaled with the values of the fitted curves at the maximum sampled values of σ_d and C_l justifying the chosen fitting functions. Each data point has been divided by the value of the fitting function at respective the maximum input parameter $\langle b \rangle_\infty^{\mathrm{fit}}(C_l^{\max})$, and $\langle b \rangle_\infty^{\mathrm{fit}}(\sigma_d^{\max})$ for $\langle b \rangle_\infty^{\mathrm{data}}(\sigma_d)$. Similar collapses could be observed using other reference points, which evidences the qualitative equivalence of the curves.

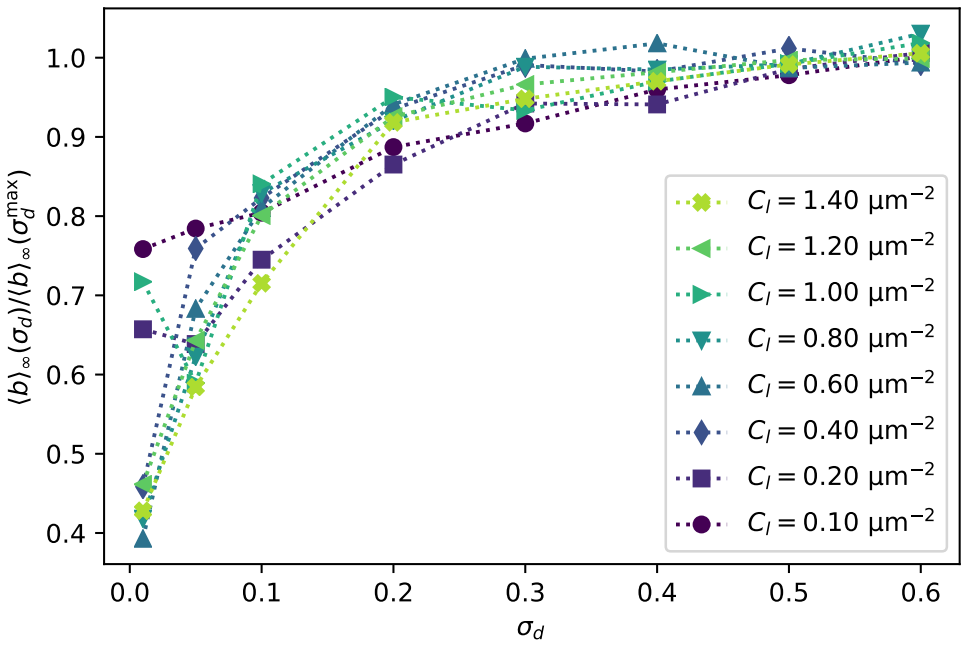

(a)

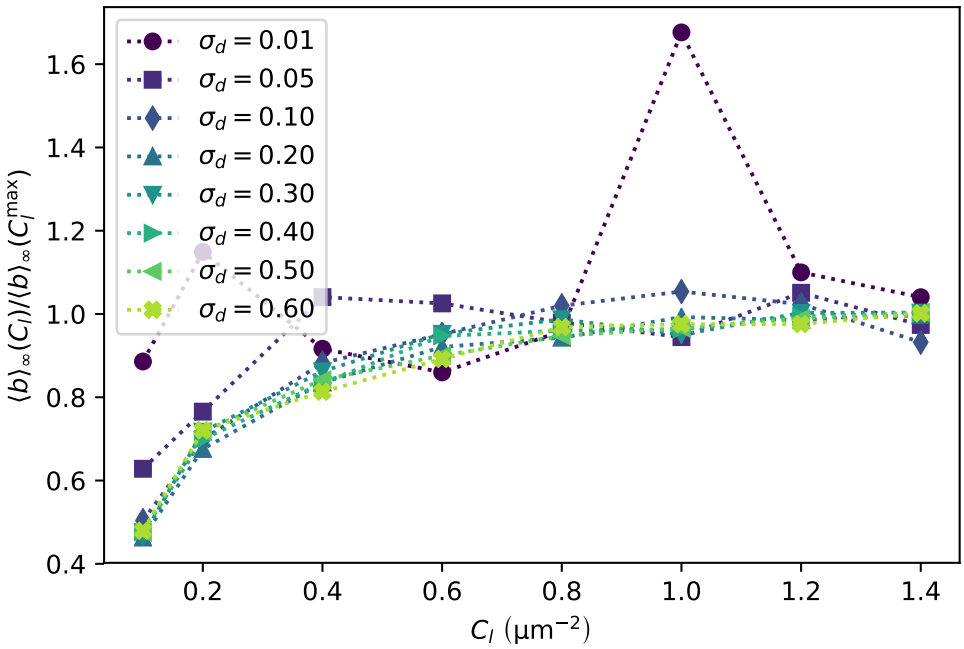

(b)

Figure 18: Normalized data (cf. Figure 17). The first plot (a) contains $\langle b\rangle_\infty^{\text{data}}(C_l)/\langle b\rangle_\infty^{\text{fit}}(C_l^{\max})$ for different particle concentrations σ_d with $C_l^{\max} = 1.4$. The second plot (b) shows the different curves of $\langle b\rangle_\infty^{\text{data}}(\sigma_d)/\langle b\rangle_\infty^{\text{fit}}(\sigma_d^{\max})$, where the asymptotic value is approximately reached at $\sigma_d^{\max} = 0.6$.

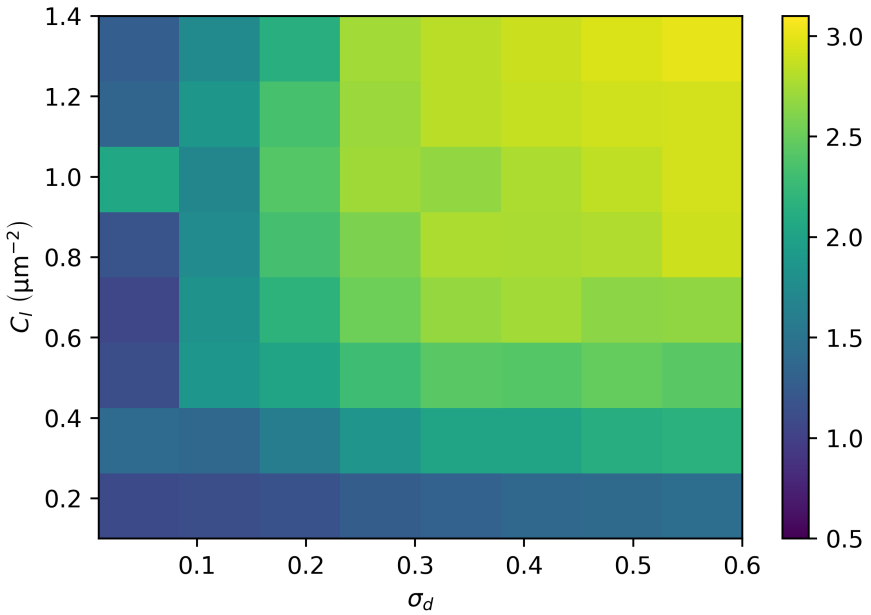

Figure 19: Heat map summing up the asymptotic values $\langle b \rangle_\infty$ of the average coordination numbers depending on the input parameters σ_d and C_l

Further, the results can be summarized in a two-dimensional heat map for $\langle b \rangle_\infty$ with the two parameters σ_d and C_l as input shown in Figure 19. Both Figure 17 (with similar growth behaviour in 17a as well as 17b) and Figure 19 suggest a symmetric dependence on linker concentration C_l and particle concentration σ_d for the system configuration after saturation with an overall asymptotic limit of $\langle b \rangle_\infty^{\text{data}}(C_l^{\max}, \sigma_d^{\max}) \approx 3$. This apparently low upper boundary for the effective valence will be discussed in detail below. At this point we can obtain a phenomenological model for $\langle b \rangle_\infty$ by taking profit of the behavior observed in the simulation results. A simple way to define a symmetric function with respect to σ_d and C_l is to factorize the limited growth function (13) for each of these parameters and perform a fit to the simulation data presented in Figure 19:

$$\langle b \rangle_\infty^{\text{fit}}(C_l, \sigma_d) = s^* \cdot \left(1 - \frac{1}{1 + (C_l / C_l^{0,*})^{p_1^*}}\right) \cdot \left(1 - \frac{1}{(1 + (\sigma_d / \sigma_d^{0,*})^{p_2^*}}\right) \tag{14}$$

The fit was performed by applying an unconstrained nonlinear least squares minimization. The results of the fitted function, whose parameters are $s^* \approx 17.7$, $\sigma_d^{0,*} \approx 4.3 \cdot 10^{-4}$, $p_1^* \approx 2.7 \cdot 10^{-2}$, $C_l^{0,*} \approx 0.213$, $p_2^* \approx 1.75$, shown in Figure 20, whereas their relative errors compared to the simulation data are shown in Figure 21. The latter are reasonably small for most of the sampled parameters space, except for the lowest value of σ_d, where the presence of outliers in the simulation data is notorious.

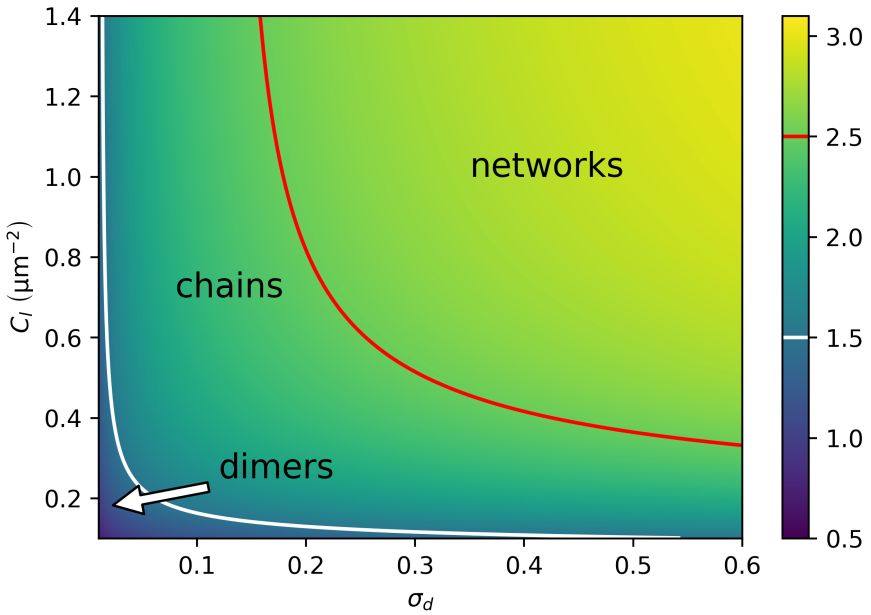

Figure 20: Reconstructed heat map obtained with a fitted 2D function depending on σ_d and C_l. The white line roughly marks the system's transition from suspension dominated dimers to the particles assembled into chains at $\langle b \rangle_\infty^{\text{fit}}(\sigma_d, C_l) = 1.5$. Respectively, the red line approximately marks the system's transition from chains to networks at $\langle b \rangle_\infty^{\text{fit}}(\sigma_d, C_l) = 2.5$.

The fitted model presented in Figure 20 not only approximates rather well the simulation data, but also allows for estimating the boundaries between different dominant structures. Taking $\langle b \rangle_\infty \approx 1.5$ as the boundary between dimers and linear chains, we can see that the former are limited to a narrow region in the limit of very low particle and linker concentrations. The region in which chains are dominant spans from low to intermediate values of σ_d and C_l, whereas more compact network structures, roughly bounded by $\langle b \rangle_\infty \approx 2.5$, appear at large concentrations.

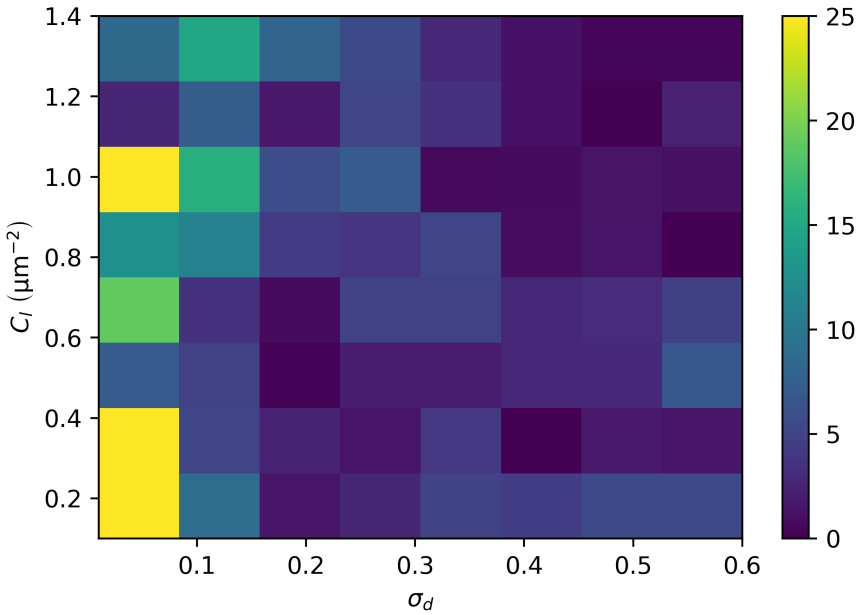

Figure 21: The relative error in % for the fit shown in Figure 20 obtained using the data plotted in Figure 19. The discrepancy between the fitted function $\langle b \rangle_\infty^{\mathrm{fit}}(\sigma_d, C_l)$ and its input data $\langle b \rangle_\infty^{\mathrm{data}}(\sigma_d, C_l)$ is reasonably low except for very low particle concentrations as expected since these values result from insufficiently long simulation runs and therefore hold some inaccuracy.

Looking at the particle self-assembly structures in detail, it is worth noticing that the average number of patches per particle never exceeds 3. This is due to the binary nature of the suspension. Since the A-type is only able to form bonds with their compatible A'-particles (cf. Figure 22b), the ground state structure is the square lattice, whereas other networks with higher coordination, such as the triangular lattice, are frustrated. The measured average coordination does not reach the ideal value corresponding to the square lattice due to the finite size of the clusters. The latter forces the existence of cluster boundaries, in which the particles necessarily miss some of their potential neighbors.

At very low concentrations of particles and/or linkers the majority of particles can only end up forming dimers corresponding to $\langle b \rangle_\infty \approx 1$ which is pictured in the first simulation snapshot of Figure 23 showing different systems at the end of a simulation run. In that case, the particles have either very few linkers or they are too diluted to meet more particles before their free linkers get exhausted. So once they meet one partner, all the linkers of the two particles get trapped in their patch and the particles become inert before meeting other possible bonding partners. The probabilities (cf. Fig 24) for systems with a low particle concentration and/or a low linker concentration to reach high $\langle b \rangle_\infty$ is almost nonexistent. Figure 23a also shows a high amount of active (non-inert) particles that still have free linkers and singlets confirming that the simulations for σ_d have not reached a fully saturated configuration. The significant amount of active particles

in simulation snapshots with high linker concentrations will be explained in the next subsection and does not question the final structures. If the monolayer contains a good amount of chains on average most particles have connections to two other particles, *i.e.*, $\langle b \rangle_\infty \approx 2$ (shown in the second and third picture of Figure 23). But when it comes to networks the square lattice configuration with alternating particle types (A and A') appears to be the only possible way for the system to form dense clusters like the one in the last picture of Figure 23. The particles need to form a chessboard due to their compatibility and energetic/entropic preferences, it represents the ground state of the system explaining the asymptotic trends for both $\langle b \rangle_\infty^{\mathrm{data}}(\sigma_d)$ as well as $\langle b \rangle_\infty^{\mathrm{data}}(C_l)$.

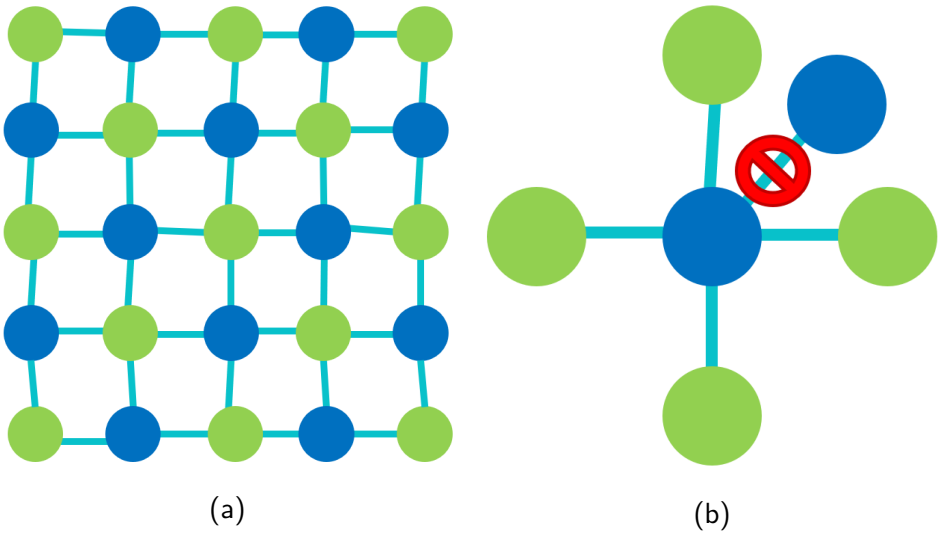

(a) (b)

Figure 22: (a) Chess board cluster for the binary DNACC mixture: The only possible network formation. (b) Zoom in one vertex with illustrating the forbidden bond.

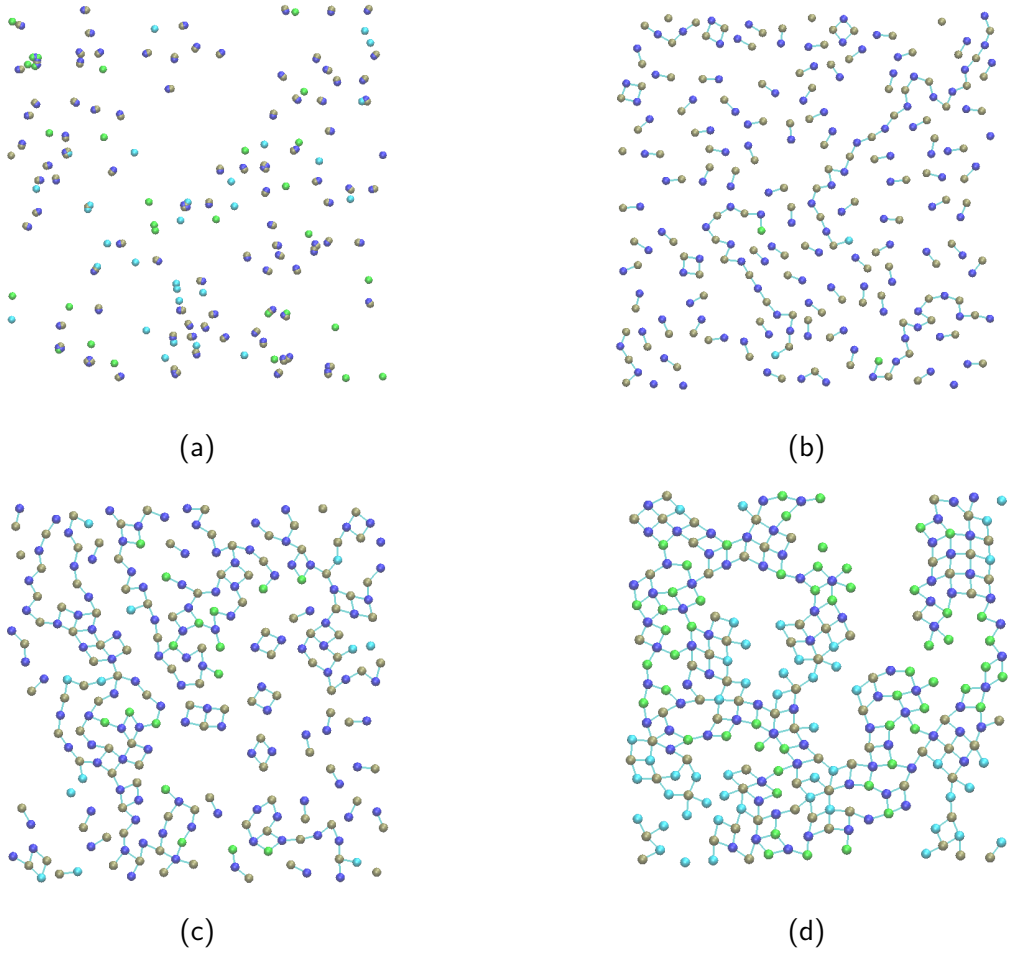

Figure 23: Snapshots of 4 different systems after self-assembly with inert A-particles in dark blue, non-inert A-particles in light blue, respectively A'-particles in dark and light green. Particle sizes have been increased in (a) and decreased in (b) to (d) with respect to their actual value in order to ease the visualization. The first snapshot (a) with parameters $\sigma_d = 0.01$, $C_l = 0.6\,\mu\mathrm{m}^{-2}$ mainly contains dimers and also singlets which indicates that the simulation has approached a moment close enough to saturation. With a moderate particle concentration $\sigma_d = 0.4$, $C_l = 0.1\,\mu\mathrm{m}^{-2}$ (b) some chains (colloidomers) are able to form. Raising both concentrations to $\sigma_d = 0.5$, $C_l = 0.2\,\mu\mathrm{m}^{-2}$ these chains connect into small networks (c). Looking at the extreme case (d) where both the particle and the linker concentration are set quite high $\sigma_d = 0.6$, $C_l = 1.4\,\mu\mathrm{m}^{-2}$ the networks of particles almost become one big percolating cluster occupying the box and a chessboard configuration is revealed.

A more detailed picture of these properties can be obtained from the probability distributions of $\langle b \rangle_\infty$ for different parameter values. Some selected examples are shown in Figure 24. It can be observed how the maxima of the distributions shift towards bigger coordinations as σ_d and C_l increase. Whereas at low concentrations particles are more likely to have only one or two neighbors, systems with higher linker and particle concentrations will probably contain large amounts of particles with four or three patches (see Figure 24 by the darkest curve). This corresponds to the particles in the middle of a square lattice network with 4 bonding partners

and a large portion of particles on the edges with fewer, mostly three connections corresponding to the limit $\max(\langle b \rangle_{\infty}^{\text{data}}(\sigma_d)) \approx \max(\langle b \rangle_{\infty}^{\text{data}}(C_l)) \approx 3$.

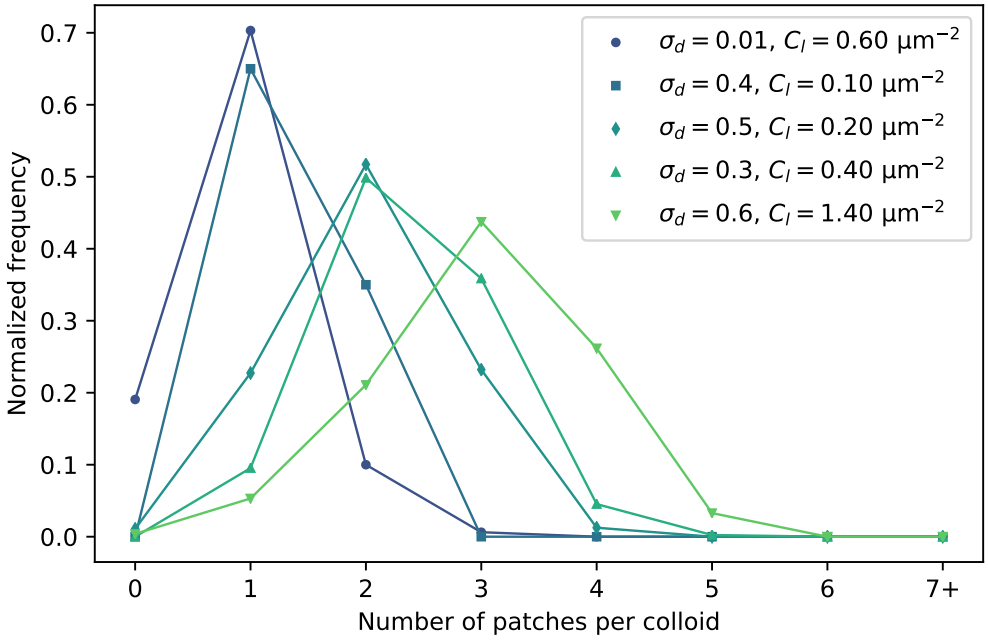

Figure 24: Probability distribution of the number of connections. This plot shows the normalized frequency of a single particle that has a certain amount of connected particles (patches) for five different system parameters corresponding to the snapshots in Figure 23. The number of patches per particle never exceeds 5 and has a moderate probability of being 4 even for very high concentrations which agrees with the chessboard ground state.

4.3 Self-assembly Dynamic Regimes and Saturation Stages

The results of Sánchez et al. [56] showed that, when varying the linker concentration, the self-assembly dynamics follows two regimes: At early times the main influence comes from the diffusion of individual particles and the formation of dimers, whereas at late times the average coordination apparently becomes qualitatively independent from C_l. Here, such observation is not only confirmed by an extended set of sampled linker concentrations but also the impact of σ_d on such behavior is clearly established. Figures 15 and 16 evidence the existence, after an initial short transient, of the two main dynamic regimes separated by an inflection point for both variations of the parameters. However, there is a significant difference in their impact on the observed dynamics: Whereas the inflection points and the approach to saturation are mostly independent of the variations of C_l (Figure 16), σ_d shortens the overall time span of the self-assembly, shifting the inflection point and the approach to saturation towards earlier times as it increases.

The dynamic regimes can also be observed in the plots containing the time evolution of

the fraction of singlets $\langle n_s \rangle / N$ and the fraction of active $\langle n_a \rangle / N$ (non-inert particles that are still able to form crosslinkers) with N again referring to the absolute number of particles in the monolayer. These parameters are shown in Figures 25a to 28b. The number of singlets which is crucial for the system's development at its early stages and its very weak/strong dependence on the linker/particle concentration shown in the examples of Figures 25 and 26 confirms that the singlets' first bonding mainly depends on the collision rate with other particles, determined by σ_d and their diffusion rate (cf. Figure 26). On the other hand, the different decreasing rates of active particles remaining in the monolayer for the various linker concentrations C_l in Figure 27 are decisive for the time it takes to reach the final saturation stage, whereas C_l has a very weak influence on it.

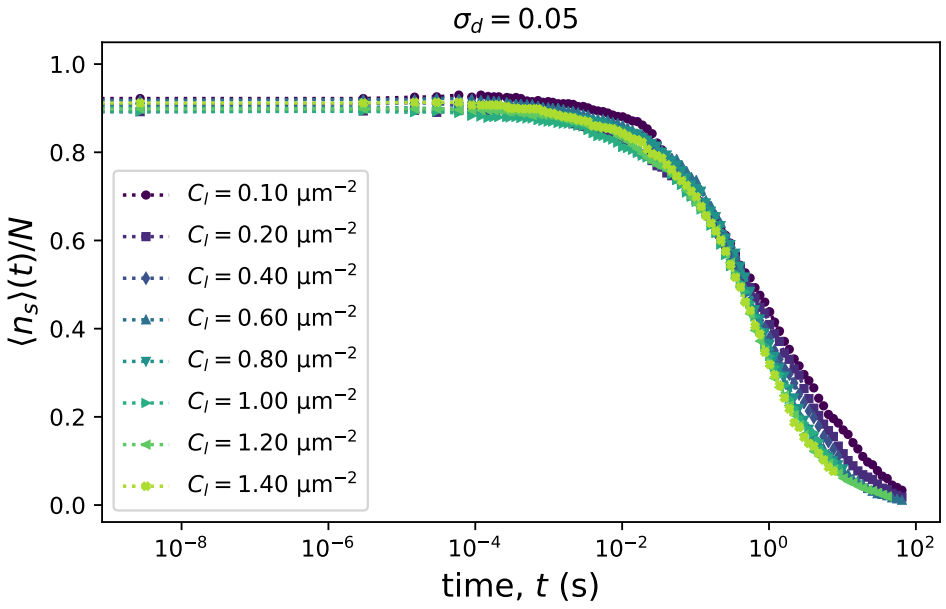

(a)

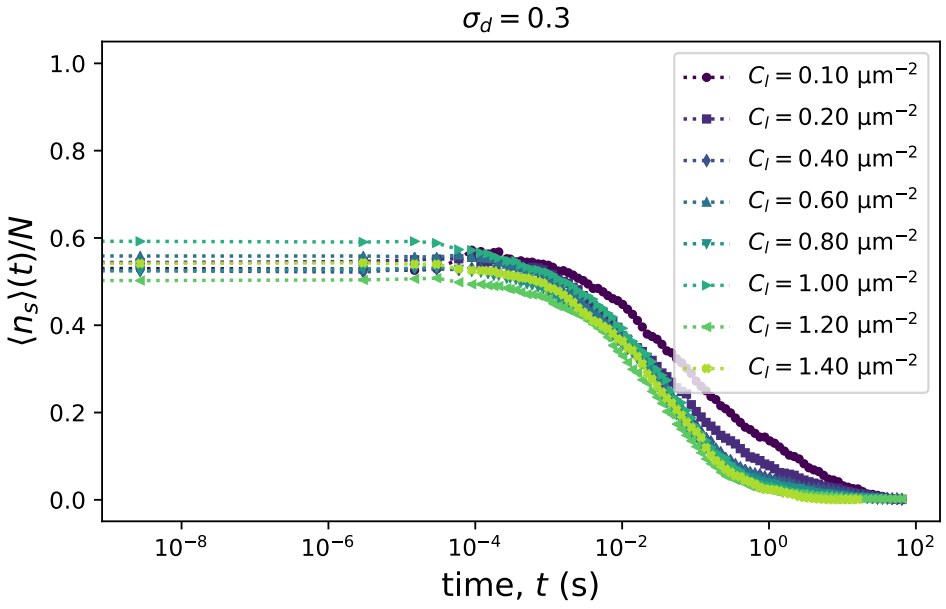

(b)

Figure 25: Average (over 5 ensembles) fraction of singlets at time t for a fixed particle area concentration $\sigma_d = 0.05$ (a) and $\sigma_d = 0.3$ (b). The plots exemplarily show the system's weak dependence on the linker concentration C_l regarding the self-assembly dynamic regimes.

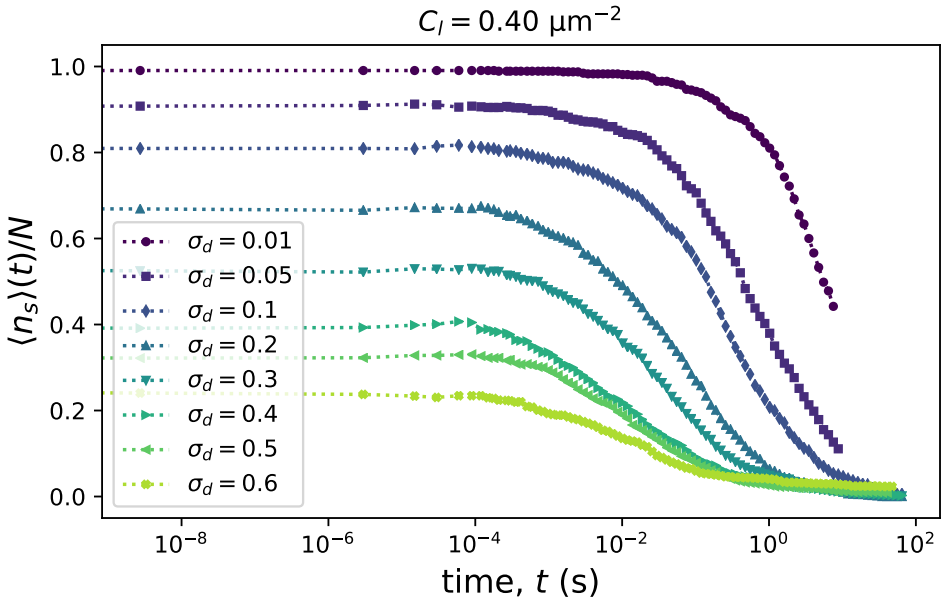

(a)

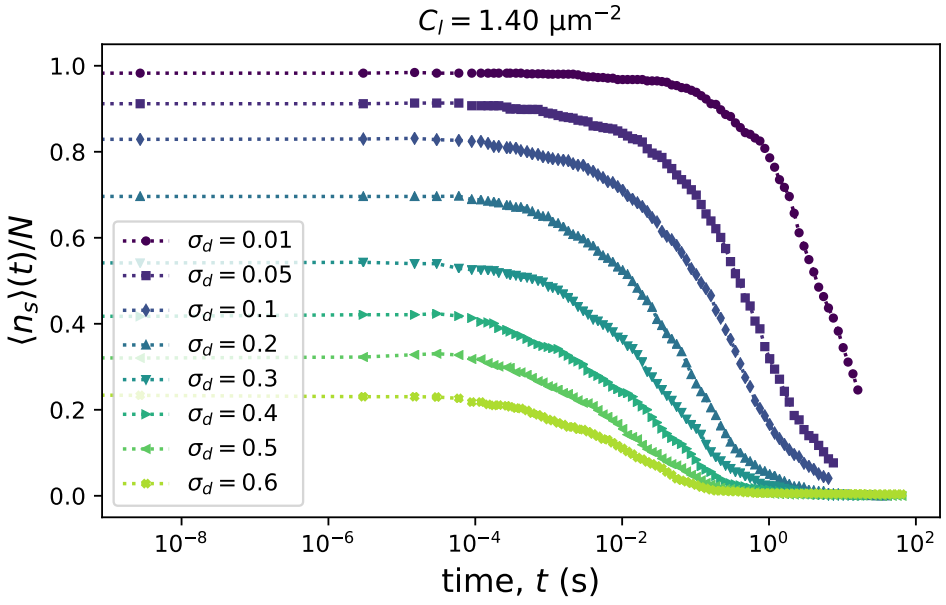

(b)

Figure 26: Average (over 5 ensembles) fraction of singlets at time t for different σ_d keeping at $C_l = 0.4\,\mu\mathrm{m}^{-2}$ (a) and $C_l = 1.4\,\mu\mathrm{m}^{-2}$ (b).

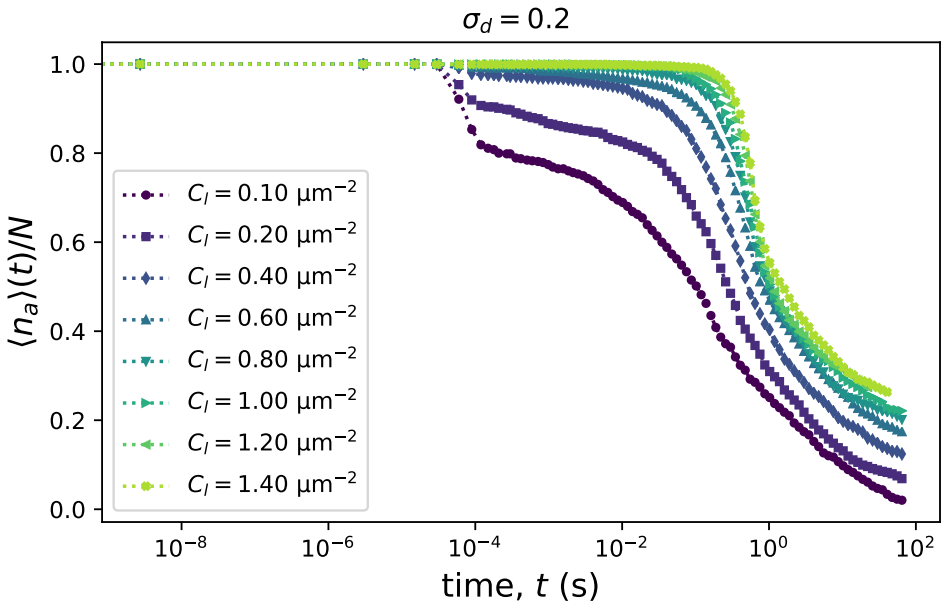

(a)

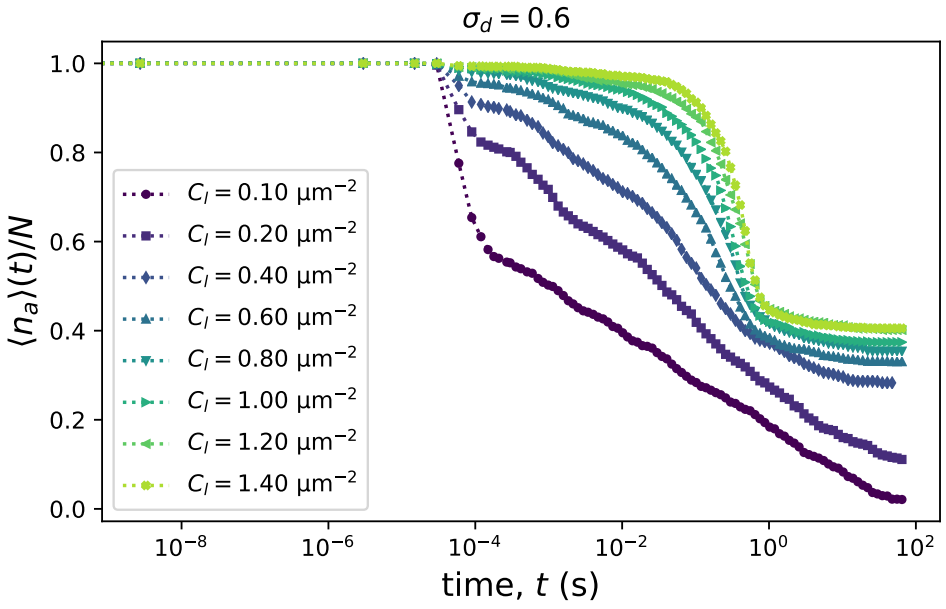

(b)

Figure 27: Time evolution of the average (over 5 ensembles) fraction of active (non-inert) particles that would be still able to form new crosslinkers for various C_l and fixed $\sigma_d = 0.2$ (a) and $\sigma_d = 0.6$ (b).

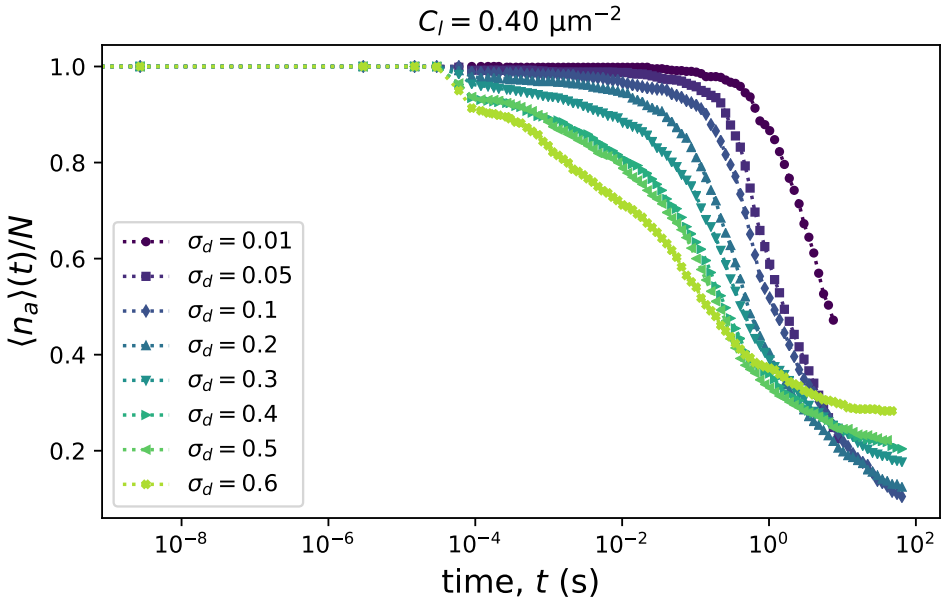

(a)

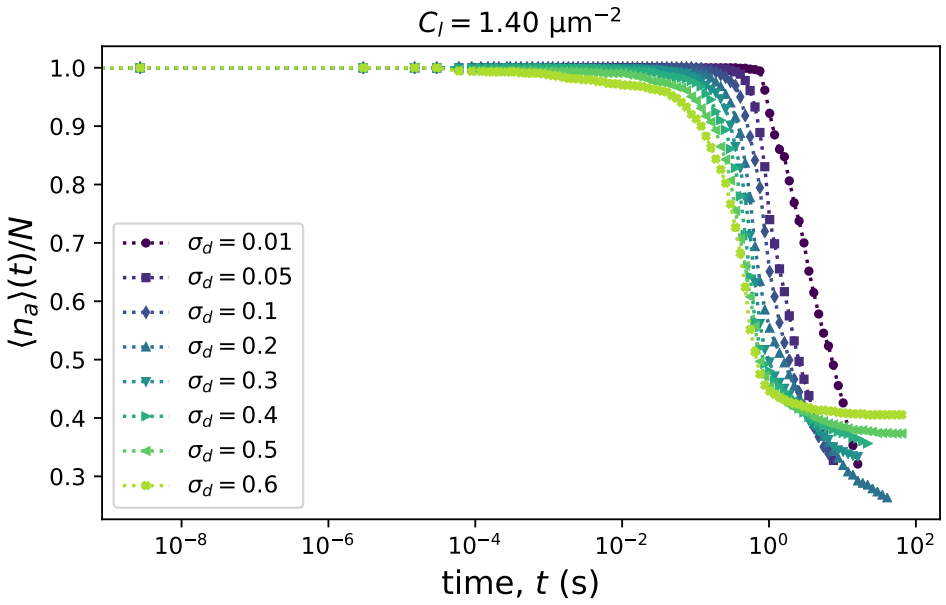

(b)

Figure 28: Time evolution of the average (over 5 ensembles) fraction of active particles with fixed $C_l = 0.4\,\mu\mathrm{m}^{-2}$ and $C_l = 1.4\,\mu\mathrm{m}^{-2}$. The active particles decrease similarly for different particle concentrations, but their fraction reaches different plateaus at the end of each simulation depending on σ_d.

Anew, the darkest curves in Figures 28 and 26 the insufficient approach to saturation at a low particle concentration $\sigma_d = 0.01$. This explains the discrepancies between the fitted model and the corresponding data points presented in Figure 21 and justifies the fitting procedures used to

minimize the impact of these inaccuracies.

Another important aspect that can be evidenced by the results of Figures 27 and 28 is the observation of very different stages reached at different concentrations regarding the fraction of non-inert particles that remain at the end of the self-assembly. On one hand, the significant fraction of non-inert particles in Figure 23a is explained by being still too far from saturation stage, and it is reasonable to assume that at longer times such fraction will tend to vanish. On the other hand, Figures 27 and 28 show that at high concentrations $\langle n_a \rangle / N$ is a non-vanishing fraction. The snapshot 23d strongly suggests that this effect is the consequence of the presence of lattice defects and frustrations. Clusters with relatively large lattice subdomains are naturally more rigid than small, loosely connected networks. Therefore, increasing the particle concentration only in principle favors the fast formation of compact lattice domains but might not help to achieve large-scale crystalline order, as it enhances frustration.

5 Conclusion

After investigating a monolayer of DNACCs by means of computer simulations using the algorithm of Sánchez et al. [56] under different conditions the impact of the two defining system parameters regarding the structural outcome of the system can be mapped out. Keeping most system parameters fixed, such as the solvent properties and the particle size, while changing the particle density σ_d and the linker concentration (number of linkers per particle) C_l made it possible to specifically look at the influence of these two crucial quantities. Examining eight different values for both input parameters of interest leads to 64 simulations which can be studied with respect to their final constellation but also the dynamics leading the system to saturation. The average coordination number, the average number of connections per particle, of a fully self-assembled system $\langle b \rangle_\infty$ shows an asymptotic behaviour when changing the linker concentration as well as the particle concentration which appears to be symmetric, *i.e.*, raising the number of linkers per particle seems to have a similar effect on the system's phase after self-assembly (dimers, chains, and networks) as increasing the particle density. Both changes are bound by the overall limit $\langle b \rangle_\infty (C_l^{\max}, \sigma_d^{\max}) \approx 3$ which corresponds to the system's ground state. Since the monolayer consists of a binary mixture where A-particles are only able to bond with A'-particles their established networks look like a chessboard where a particle in the middle of a clustered network has four neighbours, however, on average every particle connects with three other particles since most of them are situated at the edges. The dynamics while reaching a connectivity equilibrium are influenced very differently by the two concentrations. At the beginning of every simulation, a large fraction of singlets searches for possible bonding partners therefore the exact time evolution of that process is governed by the area concentration of particles σ_d. Whereas in the second time regime once already many connections have formed multi-body effects kick in and the simulation outcome is defined by the number of linkers available C_l in order to form more connections. Finally, different stages can be observed by looking at the different plateaus of the fraction of non-inert particles found in a fully saturated system. The larger networks formed at higher concentrations lead to frustration within the networks hindering crystallization on a large scale.

Regarding future works might be interesting to investigate the parameter space even further, by for example looking at different particle radii which then changes the diffusion properties but also the ratio between the linker length and the particle size. Additionally, examining various hybridization times could lead to more insight into the dynamics involved, completing the picture of how the system needs to be tuned in order to achieve the desired monolayer phase.

Appendix

A Computational Details

The code for the simulations [56] is written in Python using the ESPResSo 4.1.4 simulation package [59] to calculate the LD particle trajectories and the Python iGraph package for keeping track of a particle's type, its free linkers, and (potential) bonding partners. The computational results presented have been achieved [in part] using the Vienna Scientific Cluster (VSC). The data evaluation and all plots have been performed with Python (mainly NumPy and SciPy) as well. Finally, the visualizations of the monolayer have been created with VMD [65].

B Calculation of τ_l

The empirical formula for τ_l was developed by Chao et al. [66]. Their paper deals with proteins diffusing on the surface of a cell (its membrane) into a trap where they become immobile. The geometry of the cell with its trap is illustrated in Figure 29.

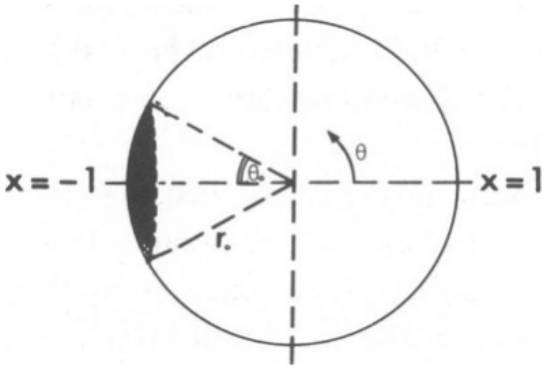

Figure 29: Geometry of the trap on the cell as well as the patch on the DNACC. The particle radius here is $R_d = r_0$ and the trap/patch in black is confined by the angle $2\theta_0$. (Taken from [66])

The surface density (the concentration) C of linkers on the particle, respectively proteins on the cell, can be described by:

$$\frac{\partial C}{\partial t} = \frac{D_l}{R_d}\frac{\partial}{\partial x}\left[(1-x^2)\frac{\partial C}{\partial x}\right], \tag{15}$$

with $x = \cos\theta$, $C = C(\theta, t)$, the initial condition $C(\theta, 0) = C(x, 0) = C_0 =$ const., and $x_0 < x \leq 1$. The trap acts as a perfect sink which leads to the boundary condition $C(x_0, t) = 0$, where $x_0 = \cos(\pi - \theta_0) = -\cos\theta_0$. This differential equation can be solved using Legendre functions. The solution is then used to calculate the number of particles $P(t) = 2\pi r_0^2 \int_{x_0}^{1} C(x,t)dx$ that

are still moving on the surface and have not reached the trap yet. The average lifetime of a protein/linker before it reaches the trap/patch is then given by $\bar{\tau} = \int_0^\infty dt \cdot t \cdot \frac{d}{dt}\left[1 - \frac{P(t)}{P(0)}\right]$. This could also be expressed as a sum of Gaussian hypergeometric functions where only the first term of the series is needed to stay within a relative error of $< 1\%$: $\bar{\tau} = K(x_0)\frac{R_d^2}{D_l}$. $K(x_0)$ is a geometry function describing the size of a trap/patch enclosed by $2\theta_0$ (see Figure 29) that can be approximated and fitted to $K(x_0) = \log_{10}\left[\frac{1}{1.55}(1+x_0)^{-2.26}\right]$ which leads directly to equation 10.

C Approximation of $S_h^0(t) \approx \langle S_h^* \rangle$

All the physical parameters used are listed in Table 1 and most values can be taken from the reference experiment [53] including the dimension of the polydimethylsiloxane droplets and their linkers which consist of $n_{ds} = 50$ double stranded DNA-base pairs and $n_{ss} = 20$ single-stranded ones, each of length $s_{ds} = 3.4 \cdot 10^{-10}$, and $s_{ss} = 5 \cdot 10^{-10}$ respectively.

Parameter	Value (S.I. units)	Reference	Dimensionless value
System thermal energy, k_BT	$4.12 \cdot 10^{-21} \cdot \mathrm{m}^2/\mathrm{s}^2$	room T	1
Particle radius, R_d	$1.5 \cdot 10^{-6}\,\mathrm{m}$	[53]	0.5
Particle core mass, m_d	$1.36 \cdot 10^{-14}\,\mathrm{kg}$	polydimethylsiloxane (PDMS) droplets at room T [53]	1
Particle viscous friction, Γ	$2.52 \cdot 10^{-8}\mathrm{m}^2/\mathrm{s}$	Stokes-Einstein equation $D_d = \frac{k_BT}{6\pi\eta R_d}$	10074
Hybridization length, d_l	$4.4 \cdot 10^{-8}\,\mathrm{m}$	estimated with respect to [53]	$1.47 \cdot 10^{-2}$
Surface diffusion constant of linkers, D_l	$2 \cdot 10^{-13}\,\mathrm{m}^2/\mathrm{s}$	[38]	$1.21 \cdot 10^4$
Background dynamic viscosity, η	$8.9 \cdot 10^{-2}\,\mathrm{kg}/(\mathrm{m}\cdot\mathrm{s})$	water at room T	1069

Table 1: Physical parameters of the simulated system. The table shows all the parameters needed to simulate the DNACCs with their respective value, the source of that quantity, and the resulting dimensionless magnitude used for Langevin Dynamics (LD). (Taken from [56])

The contour length of the crosslinkers is much smaller than the particle radius, *i.e.*, $d_l \approx 2d_{ds} + d_{ss} = 2n_{ds}s_{ds} + n_{ss}s_{ss} \approx 4.4 \cdot 10^{-8}\,\mathrm{m} << R_d \approx 1.5\,\mu\mathrm{m}$. In other words, the maximum particle distance in which hybridization is possible is very small compared to the particle radius defining the WCA-potential $U_{\mathrm{WCA}}(r)$ which is chosen to be as steep as possible without making the integration time step prohibitively small, but its barrier is still very much present at $r = R_d + d_l$. This overlap causes the particles on average to decrease the residence time of the particles within the hybridization range, making binding less likely. The WCA-potential parameters can not be changed since a steeper potential would require a very small LD time step, otherwise, the particles could coincidentally overcome the potential barrier within one LD step and experience extremely

large forces leading to crashes in the simulation. Simultaneously changing the precision and making the LD step accordingly small is also not possible since it would then be computationally unfeasible to reach interesting simulation times. The WCA-potential and the LD time step are tuned to accurately model the explicit part of the simulation, the diffusion of the particles following several approximations. When just performing simulations of the particles without their binding properties, the average time the particles stay close to each other (within the binding region $d_{cc} < 2R_d + d_l$) statistically amounts to $\delta t_h^{\mathrm{WCA}} \approx 6 \cdot 10^{-4}\,\mathrm{s}$. The mean square displacement at time t for one particle diffusing in a solvent and performing Brownian motion is given by to $\mathrm{MSD}(t) = 2nD_d t = 4D_d t$ (in a two-dimensional system $n = 2$). Therefore, this same residence time for two particles without any interaction approximately amounts to $\delta t_h^0 = d_l^2/(4D_{1,2})$ which is the diffusion time for two particles 1 and 2 with a relative diffusion coefficient $D_{1,2}$. For a single particle, the diffusion coefficient, directly related to the mean squared displacement, measures the time displacement of its random walk, *i.e.*, its effective velocity at which the particle moves away from some initial reference point. Considering two particles this reference point is the center of the second particle and therefore not fixed. If the particles start at close contact and diffuse around, statistically diffusion will increase the distance between them much faster in time than the distance of each one to the original point where they started together. The relative velocity is bound by the sum of the individual velocities. For two identical particles, the relative diffusion coefficient is given by twice their own diffusion coefficient in solvent $D_{1,2} = 2D_d$ which gives $\delta t_h^0 \approx 1.4 \cdot 10^{-3}\,\mathrm{s} \approx 2 \cdot \delta t_h^{\mathrm{WCA}}$. In order to correct for this factor of two in the binding probability and compensate for the constant bias caused by the WCA potential the hybridization region S_h^0 has to be increased by the same proportion: $S_h^* \approx 2S_h^0$. As mentioned in section 3.2, again the fact that the linkers are very small compared to the particles also justifies using a big enough LD time step coarse-graining over small particle movements/fluctuations within $d_{cc} \in [2R_d, 2R_d + d_l]$ and therefore assuming an average constant hybridization area $S_h^*(t) \mapsto \langle S_h^* \rangle \approx \pi R_d d_l$, where the average was taken with respect to $d_{cc}^{\max} = 2R_d + d_l$ and $d_{cc}^{\min} = 2R_d$ inserted into equation 6.

D Abstract (English)

In the course of this master thesis, numerous computer simulations of a monolayer of DNA-coated colloids, DNACCs - promising self-assembling supramolecular building blocks with a variety of applications such as sensors, filters, or drug delivery, have been performed and analyzed.

The system consists of a monolayer of a symmetric binary mixture of compatible DNACCs in suspension, experiencing stable self-assembly under kinetically limited conditions, that is, under a temperature below the stable DNA hybridization limit and low to moderate concentrations of particles and surface mobile linkers. Each particle has multiple mobile DNA polymers, so-called linkers, attached to its surface. They consist of an anchor allowing the linkers to diffuse

on the particle surface, a rather rigid double-stranded DNA sequence acting as a stem, and a single-stranded DNA sequence following that double helix, called a sticky end. There are equal fractions of two kinds of particles that are indistinguishable except one possesses linkers that end with a single-stranded DNA sequence A and the other category's linkers end with A'. The different sticky ends are compatible in the sense that together A- and A'-chains can form AA'-DNA via hybridization bonds. Hence, the particles in the binary mixture are able to establish connections by their linkers forming a bond, i.e., a crosslinker.

The algorithm used has been developed by Sánchez et al. who were able to validate their work by comparing the data to the experiment of McMullen et al. and observing qualitative and quantitative agreement. The computer simulations mimic the experimental DNACCs by taking into account all the relevant dynamic processes, using different approximations and a combination of explicit and implicit statistical representations depending on the involved characteristic time scales. In this way, the long experimental self-assembly times can be reached in simulations.

Making use of the advantage of simulations over experiments that parameters can be changed easily, this thesis explores the system's response when changing the number of linkers per particle and the particle area concentration, the two main parameters defining the final structures after saturation of the self-assembly process. In summary, the particles have been examined for eight different linker concentrations paired with eight particle area concentrations, exploring a parameter space beyond available experimental data.

Looking at the time evolution of the average coordination number $\langle b \rangle(t)$, *i.e.*, the average number of connections per particle, changing the linker and the particle concentration has a tremendous impact on both the configurations after self-assembly and also on the dynamics when reaching the final structures. The characteristic asymptotic limits $\langle b \rangle_\infty$ for every $\langle b \rangle(t)$ curve grow with the concentration of particles and/or linkers, showing a similar qualitative time evolution corresponding to a limited growth process. The limitations refer to an overall ground state which looks like a chessboard due to the binary nature of the system. The structural phase diagram as a function of particle and linker concentrations is determined from the simulation data and a simple phenomenological model is fitted, easing the identification of the boundaries between different structural regions, dominated by either dimers, linear chains, or more compact structures.

Finally, the assembling dynamics of each system show two time regimes that are impacted differently by the two changing parameters. Initially, the formation of connections is governed by the particle density whereas later on once certain configurations amongst the particles have been established multi-body effects take over, defining how the system is driven to saturation. In general, the concentration of linkers has a quantitative impact on the self-assembly, whereas particle concentration determines its overall time span. For the latter parameter, high concen-

trations favor the fast formation of compact structures but this also promotes lattice defects and frustration, limiting the range of the crystalline order.

E Abstract (German)

Im Rahmen dieser Masterarbeit wurden zahlreiche Computersimulationen von einer Schicht aus DNA-ummantelten Kolloiden – vielversprechenden, sich selbst organisierenden, supramolekularen Bauteilen mit einer Vielzahl an Applikationen wie Sensoren, Filter, oder gezielter medikamentöser Wirkstoffabhabe, durchgeführt.

Das System besteht aus einer Einzelschicht einer symmetrischen binaren Mischung an kompatiblen DNACCs in einer Lösung und erfährt stabile Selbstoranisation unter kinetisch limitierten Bedingungen, d.h, bei Temperaturen unter dem stabilen DNA-Hybridisierungslimit und bei geringen bis moderaten Konzentrationen von Partikeln und Oberflächenlinkern. An der Oberfläche eines jeden Teilchens sind DNA-Polymere, sogenannte Linker, befestigt. Jedes Teilchen besitzt mehrere mobile DNA-Polymere, sogenannte Linker, die auf seiner Oberfläche befestigt sind. Sie bestehen aus einem Anker, der es ihnen erlaubt entlang der Teilchenoberfläche zu diffundieren, aus einer recht starren doppelsträngigen DNA-Sequenz, die als Verbindungsstück dient, und einer einzelsträngigen DNA-Sequenz am Ende der Doppelhelix. Es gibt gleich große Teile an zwei Arten von Partikel, die ununterscheidbar sind bis auf die Tatsache, dass die eine Linker besitzt, die mit der DNA-Sequenz A enden, und die Linker der anderen Kategorie enden mit A‘. Die verschiedenen Linkerenden sind kompatible im Sinne, dass die beiden A- und A‘-Ketten gemeinsam AA‘-DNA mithilfe von Wasserstoffbrückenbindungen bilden können. Daher ist es den Teilchen möglich, Verbindungen miteinander einzugehen, indem ihre Linker sich zusammenschließen zu einem Crosslinker.

Der verwendete Algorithmus wurde von Sánchez et al. entwickelt, die Forscher konnten ihre Arbeit validieren durch den Vergleich der Daten mit dem Experiment von McMullen et al, wo sie qualitative und quantitative Übereinstimmung beobachten konnten. Die Computersimulationen imitieren die experimentellen DNACCs unter Berücksichtigung aller relevanten Prozesse, wobei verschiedene Approximierungen und eine Kombination aus expliziten und impliziten statistischen Repräsentationen abhängig von den charakteristischen Zeitskalen benutzt wurden. Auf diese Weise können lange experimentelle Selbstorganisiationszeiten in Simulationen erreicht werden.

Der Vorteil von Simulationen gegenüber Experimenten ist, dass alle Parameter ganz einfach geändert werden können. Diese Masterarbeit macht sich dies zunutze und erforscht die Reaktion des Systems, wenn die Anzahl der Linker pro Teilchen und die Teilchenkonzentration, die beiden entscheidenden Parameter bezüglich der Teilchenkonstellation nach der Selbstorganisation, verändert werden. Zusammenfassend werden die Partikel für acht verschiedene linker Konzentrationen gepaart mit acht Teilchenkonzentrationen untersucht, wobei ein Parameterraum jenseits

der derzeit verfügbaren experimentellen Daten erforscht werden kann.

Die Zeitentwicklung der mittleren Koordinationsnummber betrachtend, d.h. der mittleren Anzahl an Verbindungen pro Teilchen, hat die Änderung der Linker- und Partikelkonzentration einen großen Einfluss auf die Konfiguration nach der Selbstzusammensetzung, aber auch auf die Dynamiken beim Erreichen finaler Strukturen. Die charakteristischen asymptotischen Limits für jede mittlere Koordinationsnummer-Kurve wachsen mit der Konzentration von Partikeln und/oder Linkern, es zeigt sich eine ähnliche Zeitentwicklung korrespondierend mit dem limitierten Wachstumsprozess. Die Limitierungen beziehen sich auf einen allgemeinen Grundzustand, der wie ein Schachbrett aussieht aufgrund der binären Natur des Systems. Das strukturelle Phasendiagramm ist bestimmt durch die simulierten Daten und ein phänomenologisches Modell wird gefittet, um die Identifikation der Grenzen zwischen verschiedenen Strukturregionen zu erleichtern, dominiert bei entweder Dimeren, Ketten, oder kompakteren Strukturen.

Schließlich zeigen die Dynamiken des Zusammensetzens von jedem System zwei verschiedene zeitliche Regime, die unterschiedlich beeinflusst werden von den beiden sich ändernden Parametern. Zu Beginn ist die Formation von Verbindungen bestimmt von der Teilchendichte, wobei später, wenn sich bestimmte Konfigurationen unter den Teilchen herausgebildet haben, Mehrkörper-Effekte übernehmen und entscheiden, wie das System Saturation erreicht. Im Allgemeinen hat die Konzentration von Linkern einen quantitativen Einfluss auf die Selbstorganisation, wobei die Teilchenkonzentration die gesamte Zeitspanne bestimmt. Bezüglich des letztgenannten Parameters begünstigen hohe Konzentrationen eine Formation von kompakten Strukturen, aber das fördert auch Gitterdefekte und Frustration, wodurch der Bereich der Kristallisation limitiert wird.

References

[1] Jean-Marie Lehn. Perspectives in Chemistry—Steps towards Complex Matter. *Angewandte Chemie International Edition*, 52(10):2836–2850, 2013.

[2] Vinod K. Wadhawan. SELF-ASSEMBLY AND SELF-ORGANIZATION OF MATTER. In *Smart Structures: Blurring the Distinction Between the Living and the Nonliving*. Oxford University Press, 10 2007.

[3] Eric Bonabeau, Marco Dorigo, and Guy Theraulaz. *Swarm Intelligence: From Natural to Artificial Systems*. Oxford University Press, 10 1999.

[4] Peter J. Cragg. *Supramolecular Chemistry: From Biological Inspiration to Biomedical Applications*. Springer Netherlands, Dordrecht, 2010.

[5] Zhenli Zhang and Sharon Glotzer. Self-assembly of patchy particles. *Nano Letters*, 4, 07 2004.

[6] Serge Ravaine and Etienne Duguet. Synthesis and assembly of patchy particles: Recent progress and future prospects. *Current Opinion in Colloid and Interface Science*, 30:45–53, 2017.

[7] Emanuela Bianchi, Barbara Capone, Ivan Coluzza, Lorenzo Rovigatti, and Peter Oostrum. Limiting the valence: Advancements and new perspectives on patchy colloids, soft functionalized nanoparticles and biomolecules. *Phys. Chem. Chem. Phys.*, 19, 05 2017.

[8] M. Wang and M. Thanou. Targeting nanoparticles to cancer. *Pharmacological Research*, 62(2):90–99, 2010. Towards clinical applications of nanoscale medicines.

[9] Andrew Shipway, Evgeny Katz, and Itamar Willner. Nanoparticle Arrays on Surfaces for Electronic, Optical, and Sensor Applications. *Chemphyschem : a European journal of chemical physics and physical chemistry*, 1:18–52, 08 2000.

[10] Sachin Kinge, Mercedes Crego-Calama, and David Reinhoudt. Self-Assembling Nanoparticles at Surfaces and Interfaces. *Chemphyschem : a European journal of chemical physics and physical chemistry*, 9:20–42, 01 2008.

[11] Stefano Angioletti-Uberti, Bortolo Mognetti, and Daan Frenkel. Theory and Simulation of DNA-Coated Colloids: a Guide for Rational Design. *Phys. Chem. Chem. Phys.*, 18, 01 2016.

[12] Ludovico Cademartiri and Kyle J. M. Bishop. Programmable self-assembly. *Nature materials*, 14 1:2–9, 2015.

[13] P.I.C. Teixeira and J.M. Tavares. Phase behaviour of pure and mixed patchy colloids — theory and simulation. *Current Opinion in Colloid Interface Science*, 30:16–24, 2017.

[14] Orlin D. Velev and Eric. Kaler. In situ assembly of colloidal particles into miniaturized biosensors. *Langmuir*, 15:3693–3698, 1999.

[15] Chad A Mirkin, Robert L. Letsinger, Robert C. Mucic, and James J. Storhoff. A DNA-based method for rationally assembling nanoparticles into macroscopic materials. *Nature*, 382(6592):607–609, August 1996.

[16] W. Rogers, William Shih, and Vinothan Manoharan. Using DNA to program the self-assembly of colloidal nanoparticles and microparticles. *Nature Reviews Materials*, 1:16008, 03 2016.

[17] Stef van der Meulen and Mirjam Leunissen. Solid Colloids with Surface-Mobile DNA Linkers. *Journal of the American Chemical Society*, 135, 09 2013.

[18] Sabine H.L. Klapp. Collective dynamics of dipolar and multipolar colloids: From passive to active systems. *Current Opinion in Colloid and Interface Science*, 21:76–85, 2016.

[19] Mena Youssef, Theodore Hueckel, Gi-Ra Yi, and Stefano Sacanna. Shape-shifting colloids via stimulated dewetting. *Nature Communications*, 7, 2016.

[20] Yufeng Wang, Yu Wang, Dana R. Breed, Vinothan N. Manoharan, Lang Feng, Andrew Hollingsworth, Marcus Weck, and David Pine. Colloids with valence and specific directional bonding. *Nature*, 491:51–55, 11 2012.

[21] C.R. Laramy, M.N. O'Brien, and C.A. Mirkin. Crystal engineering with DNA. *Nat Rev Mater*, 4:201–224, 03 2019.

[22] Tianran Zhang, Dengping Lyu, Wei Xu, Yijiang Mu, and Yufeng Wang. Programming Self-Assembled Materials With DNA-Coated Colloids. *Frontiers Media SA*, 2021.

[23] Dmytro Nykypanchuk, Mathew M. Maye, Daniel van der Lelie, and Oleg Gang. DNA-Based Approach for Interparticle Interaction Control. *Langmuir*, 23(11):6305–6314, 2007. PMID: 17447797.

[24] Matthew Jones, Robert Macfarlane, Byeongdu Lee, Jian Zhang, Kaylie Young, Andrew Senesi, and Chad Mirkin. *DNA-Nanoparticle Superlattices Formed from Anisotropic Building Blocks**, pages 601–613. 07 2020.

[25] Iliya D. Stoev, Alessio Caciagli, Anasua Mukhopadhyay, Christopher Ness, and Erika Eiser. Bulk rheology of sticky dna-functionalized emulsions. *Phys. Rev. E*, 104:054602, Nov 2021.

[26] Lorenzo Di Michele and Erika Eiser. Developments in understanding and controlling self assembly of dna-functionalized colloids. *Phys. Chem. Chem. Phys.*, 15:3115–3129, 2013.

[27] Valeria Milam, Amy Hiddessen, John Crocker, David Graves, and Daniel Hammer. Dna-driven assembly of bidisperse, micron-sized colloids. *Langmuir*, 19, 10 2003.

[28] Paul L. Biancaniello, Anthony J. Kim, and John C. Crocker. Colloidal interactions and self-assembly using dna hybridization. *Phys. Rev. Lett.*, 94:058302, Feb 2005.

[29] Selective, controllable, and reversible aggregation of polystyrene latex microspheres via DNA hybridization., author=Phillip H. Rogers and Eric Michel and Carl A. Bauer and Stephen Vanderet and Daniel Hansen and Bradley K. Roberts and Antoine Calvez and Jackson B Crews and Kwok O Lau and Alistair Wood and David J. Pine and Peter V. Schwartz. *Langmuir : the ACS journal of surfaces and colloids*, 21 12:5562–9, 2005.

[30] Anthony J. Kim, Paul Biancaniello, and John C. Crocker. Engineering dna-mediated colloidal crystallization. *Langmuir : the ACS journal of surfaces and colloids*, 22 5:1991–2001, 2006.

[31] Lucia Parolini, Bortolo Matteo Mognetti, Jurij Kotar, Erika Eiser, Pietro Cicuta, and Lorenzo Di Michele. Volume and porosity thermal regulation in lipid mesophases by coupling mobile ligands to soft membranes. *Nature Communications*, 6, 2014.

[32] Maik Hadorn, Eva Boenzli, and Martin Michael Hanczyc. Specific and Reversible DNA-Directed Self-Assembly of Modular Vesicle-Droplet Hybrid Materials. *Langmuir : the ACS journal of surfaces and colloids*, 32 15:3561–6, 2016.

[33] Yan Xiong, Zhiwei Lin, Deniz Mostarac, Brian Minevich, Qiuyuan Peng, Guolong Zhu, Pedro A Sánchez, Sofia S. Kantorovich, Yonggang Ke, and Oleg Gang. Divalent multilinking bonds control growth and morphology of nanopolymers. *Nano Letters*, 21:10547 – 10554, 2021.

[34] Rémi Dreyfus, Mirjam E. Leunissen, Roujie Sha, Alexei V. Tkachenko, Nadrian C. Seeman, David J. Pine, and Paul M. Chaikin. Simple quantitative model for the reversible association of dna coated colloids. *Phys. Rev. Lett.*, 102:048301, Jan 2009.

[35] Maik Hadorn, Eva Boenzli, Kristian Tølbøl Sørensen, Harold Fellermann, Peter Eggenberger Hotz, and Martin Michael Hanczyc. Specific and reversible dna-directed self-assembly of oil-in-water emulsion droplets. *Proceedings of the National Academy of Sciences*, 109:20320 – 20325, 2012.

[36] Lang Feng, Rémi Dreyfus, Ruojie Sha, Nadrian C. Seeman, and Paul M. Chaikin. DNA Patchy Particles. *Advanced Materials*, 25(20):2779–2783, 2013.

[37] Lang Feng, Lea-Laetitia Pontani, Rémi Dreyfus, Paul Chaikin, and Jasna Brujic. Specificity, flexibility and valence of DNA bonds guide emulsion architecture. *Soft Matter*, 9:9816–9823, 2013.

[38] Darshana Joshi, Dylan Bargteil, Alessio Caciagli, Jérôme Burelbach, Zhongyang Xing, André Nunes, Diogo Pinto, Nuno Araujo, Jasna Brujic, and Erika Eiser. Kinetic control of the coverage of oil droplets by DNA-functionalized colloids. *Science Advances*, 2, 08 2016.

[39] Yin Zhang, Angus McMullen, Lea-Laetitia Pontani, Xiaojin He, Ruojie Sha, Nadrian C. Seeman, Jasna Brujic, and Paul M. Chaikin. Sequential self-assembly of DNA functionalized droplets. *Nature Communications*, 8:21, June 2017.

[40] Alessio Caciagli, M Zupkauskas, Aviad Levin, Tuomas P. J. Knowles, Clément Mugemana, Nico Bruns, Thomas O'Neill, William J. Frith, and Erika Eiser. DNA-Coated Functional Oil Droplets. *Langmuir : the ACS journal of surfaces and colloids*, 34 34:10073–10080, 2017.

[41] Rémi Dreyfus, Mirjam E. Leunissen, Roujie Sha, Alexei Tkachenko, Nadrian C. Seeman, David J. Pine, and Paul M. Chaikin. Aggregation-disaggregation transition of dna-coated colloids: Experiments and theory. *Phys. Rev. E*, 81:041404, Apr 2010.

[42] Stefano Angioletti-Uberti, Bortolo Matteo Mognetti, and Daan Frenkel. Re-entrant melting as a design principle for dna-coated colloids. *Nature materials*, 11 6:518–22, 2012.

[43] Yu Wang, Yufeng Wang, Xiaolong Zheng, Étienne Ducrot, Yodh Jeremy S., Marcus Weck, and David J. Pine. Crystallization of DNA-coated colloids. *Nat Commun*, 120:7253, June 2015.

[44] Lang Feng, Léa-Laetitia Pontani, Rémi Dreyfus, Paul M. Chaikin, and Jasna Brujic. Specificity, flexibility and valence of dna bonds guide emulsion architecture. 2013.

[45] In-Seong Jo, Saerom Lee, Jintao Zhu, Tae Soup Shim, and Gi-Ra Yi. Soft patchy micelles. *Current Opinion in Colloid Interface Science*, 30:97–105, 2017.

[46] Stefano Angioletti-Uberti, Patrick Varilly, Bortolo M. Mognetti, and Daan Frenkel. Mobile Linkers on DNA-Coated Colloids: Valency without Patches. *Phys. Rev. Lett.*, 113:128303, Sep 2014.

[47] Lorenzo Di Michele, Francesco Varrato, Jurij Kotar, Simon H Nathan, Giuseppe Foffi, and Erika Eiser. Multistep kinetic self-assembly of DNA-coated colloids. *Nature Communications*, 4, 2013.

[48] Mirjam E. Leunissen and Daan Frenkel. Numerical study of DNA-functionalized microparticles and nanoparticles: explicit pair potentials and their implications for phase behavior. *The Journal of chemical physics*, 134 8:084702, 2011.

[49] Evan Pretti, Runfang Mao, and Jeetain Mittal. Modelling and simulation of DNA-mediated self-assembly for superlattice design. *Molecular Simulation*, 45(14-15):1203–1210, 2019.

[50] Patrick Varilly, Stefano Angioletti-Uberti, Bortolo Matteo Mognetti, and Daan Frenkel. A general theory of DNA-mediated and other valence-limited colloidal interactions. *The Journal of chemical physics*, 137 9:094108, 2012.

[51] Bianca M. Mladek, Julia Fornleitner, Francisco J. Martinez-Veracoechea, Alexandre Dawid, and Daan Frenkel. Procedure to construct a multi-scale coarse-grained model of DNA-coated colloids from experimental data. *Soft Matter*, 9:7342–7355, 2013.

[52] Hao Hu, Pablo Sampedro Ruiz, and Ran Ni. Entropy Stabilizes Floppy Crystals of Mobile DNA-Coated Colloids. *Phys. Rev. Lett.*, 120:048003, Jan 2018.

[53] Angus McMullen, Miranda Holmes-Cerfon, Francesco Sciortino, Alexander Y. Grosberg, and Jasna Brujic. Freely Jointed Polymers Made of Droplets. *Phys. Rev. Lett.*, 121:138002, Sep 2018.

[54] Gaurav Mitra, Chuan Chang, Angus McMullen, Daniela Puchall, Jasna Brujic, and Glen M. Hocky. A coarse-grained simulation model for colloidal self-assembly via explicit mobile binders. *Soft Matter*, 19:4223–4236, 2023.

[55] Stephan Jan Bachmann, Marius Petitzon, and Bortolo Matteo Mognetti. Bond formation kinetics affects self-assembly directed by ligand–receptor interactions. *Soft Matter*, 12:9585–9592, 2016.

[56] Pedro A. Sánchez, Alessio Caciagli, Sofia S. Kantorovich, and Erika Eiser. Kinetically limited valence of colloidal particles with surface mobile DNA linkers. *Journal of Molecular Liquids*, 382:121895, 2023.

[57] M. P. Allen and D. J. Tildesley. *Computer Simulation of Liquids*, volume 2. Oxford University Press, 2017.

[58] Daan Frenkel and Berend Smit. *Understanding Molecular Simulation*. Academic Press, Inc., USA, 2nd edition, 2001.

[59] Weik, F. and Weeber, R. and Szuttor, K. and Breitsprecher, K. and J., de Graaf and Kuron, M. and Landsgesell, J. and Menke, H. and Sean, D. and Holm, C. Espresso 4.0 – an extensible software package for simulating soft matter systems. *The European Physical Journal Special Topics*, 03 2019.

[60] John D. Weeks, David Chandler, and Hans C. Andersen. Role of Repulsive Forces in Determining the Equilibrium Structure of Simple Liquids. , 54(12):5237–5247, June 1971.

[61] Angus McMullen, Sascha Hilgenfeldt, and Jasna Brujic. DNA self-organization controls valence in programmable colloid design. *Proceedings of the National Academy of Sciences*, 118(46):e2112604118, 2021.

[62] Ratna Katiyar and Prateek Jha. Molecular simulations in drug delivery: Opportunities and challenges. *Wiley Interdisciplinary Reviews: Computational Molecular Science*, 8:e1358, 02 2018.

[63] Wikimedia Commons. File:spherical cap diagram.tiff — wikimedia commons, the free media repository, 2022. [Online; accessed 7-April-2023].

[64] Gary S. Grest and Kurt Kremer. Molecular dynamics simulation for polymers in the presence of a heat bath. *Phys. Rev. A*, 33:3628–3631, May 1986.

[65] W. Humphrey, A. Dalke, and K. Schulten. VMD – Visual Molecular Dynamics. *Journal of Molecular Graphics*, 14:33–38, 1996.

[66] N.M. Chao, S.H. Young, and M.M. Poo. Localization of cell membrane components by surface diffusion into a "trap". *Biophysical Journal*, 36(1):139–153, 1981.